Wnt signaling mediates acquisition of blood-brain barrier properties in naïve endothelium derived from human pluripotent stem cells

Benjamin D. Gastfriend[1], Hideaki Nishihara[2], Scott G. Canfield[1†], Koji L. Foreman[1], Britta Engelhardt[2], Sean P. Palecek[1*], and Eric V. Shusta[1,3*]

[1]Department of Chemical and Biological Engineering, University of Wisconsin–Madison, Madison, WI, USA

[2]Theodor Kocher Institute, University of Bern, Bern, Switzerland

[3]Department of Neurological Surgery, University of Wisconsin–Madison, Madison, WI, USA

[†]Current affiliation: Department of Cellular and Integrative Physiology, Indiana University School of Medicine, Terre Haute, IN, USA

[*]Corresponding authors:

Prof. Eric V. Shusta
Department of Chemical and Biological Engineering
Department of Neurological Surgery
University of Wisconsin–Madison
1415 Engineering Drive
Madison, WI 53706
eshusta@wisc.edu
(608) 265-5103

Prof. Sean P. Palecek
Department of Chemical and Biological Engineering
University of Wisconsin–Madison
1415 Engineering Drive
Madison, WI 53706
sppalecek@wisc.edu
(608) 262-8931

Running title: Wnt-mediated barriergenesis in hPSC-endothelium

ABSTRACT

Endothelial cells (ECs) in the central nervous system (CNS) acquire their specialized blood-brain barrier (BBB) properties in response to extrinsic signals, with Wnt/β-catenin signaling coordinating multiple aspects of this process. Our knowledge of CNS EC development has been advanced largely by animal models, and human pluripotent stem cells (hPSCs) offer the opportunity to examine BBB development in an *in vitro* human system. Here we show that activation of Wnt signaling in hPSC-derived naïve endothelial progenitors, but not in matured ECs, leads to robust acquisition of canonical BBB phenotypes including expression of GLUT-1, increased claudin-5, and decreased PLVAP. RNA-seq revealed a transcriptome profile resembling ECs with CNS-like characteristics, including Wnt-upregulated expression of *LEF1*, *APCDD1*, and *ZIC3*. Together, our work defines effects of Wnt activation in naïve ECs and establishes an improved hPSC-based model for interrogation of CNS barriergenesis.

KEYWORDS

Endothelial cells, blood-brain barrier, barriergenesis, Wnt signaling

2

INTRODUCTION

In the central nervous system (CNS), vascular endothelial cells (ECs) are highly specialized, with complex tight junctions, expression of a spectrum of nutrient and efflux transporters, low rates of vesicle trafficking, no fenestrae, and low expression of immune cell adhesion molecules (Reese and Karnovsky, 1967; Obermeier et al., 2013). ECs bearing these attributes, often referred to as the blood-brain barrier (BBB), work in concert with the other brain barriers to facilitate the tight regulation of the CNS microenvironment required for proper neuronal function (Daneman and Engelhardt, 2017; Profaci et al., 2020). During development, the Wnt/β-catenin signaling pathway drives both CNS angiogenesis, during which vascular sprouts originating from the perineural vascular plexus invade the developing neural tube, and the coupled process of barriergenesis by which resulting ECs begin to acquire BBB properties (Liebner et al., 2008; Stenman et al., 2008; Daneman et al., 2009; Engelhardt and Liebner, 2014; Umans et al., 2017). Specifically, neural progenitor-derived Wnt7a and Wnt7b ligands signal through Frizzled receptors and the obligate co-receptors RECK and GPR124 (ADGRA2) on endothelial cells (Kuhnert et al., 2010; Cullen et al., 2011; Vanhollebeke et al., 2015; Cho et al., 2017; Eubelen et al., 2018; Vallon et al., 2018). Other ligands function analogously in the retina (Norrin) (Ye et al., 2009; Wang et al., 2012) and potentially in the dorsal neural tube (Daneman et al., 2009). Furthermore, Wnt/β-catenin signaling is required for maintenance of CNS EC barrier properties in adulthood (Tran et al., 2016), with astrocytes as a major source of Wnt7 ligands (He et al., 2018; Vanlandewijck et al., 2018; Guérit et al., 2021).

Molecular hallmarks of Wnt-mediated CNS EC barriergenesis are (i) acquisition of glucose transporter GLUT-1 expression, (ii) loss of plasmalemma vesicle-associated protein (PLVAP), and (iii) upregulation of claudin-5 (Daneman et al., 2009; Kuhnert et al., 2010; Cho et al., 2017; Umans et al., 2017; Wang et al., 2019). Notably, the Wnt-mediated switch between the

3

68   "leaky" EC phenotype (GLUT-1$^-$ PLVAP$^+$ claudin-5^{low}) and the barrier EC phenotype (GLUT-

69   1$^+$ PLVAP$^-$ claudin-5^{high}) correlates with reduced permeability to molecular tracers (Wang et al.,

70   2012; Cho et al., 2017) and is conserved in multiple contexts. For instance, medulloblastomas

71   that produce Wnt-inhibitory factors have leaky vessels (Phoenix et al., 2016). Moreover,

72   vasculature perfusing circumventricular organs is leaky due to low levels of Wnt signaling (Benz

73   et al., 2019; Wang et al., 2019). Notably, ectopic activation of Wnt in ECs of circumventricular

74   organs induces GLUT-1 and suppresses PLVAP (Benz et al., 2019; Wang et al., 2019).

75   However, similar ectopic activation of Wnt in liver and lung ECs produces only very minor

76   barriergenic effects (Munji et al., 2019), and Wnt activation in cultured primary mouse brain ECs

77   does not prevent culture-induced loss of barrier-associated gene expression (Sabbagh and

78   Nathans, 2020). The reasons for the apparent context-dependent impacts of Wnt activation in

79   ECs remain unclear and motivate systematic examination of this process in a simplified model

80   system. Further, given species differences in brain EC transporter expression (Uchida et al.,

81   2011), drug permeability (Syvänen et al., 2009), and gene expression (Song et al., 2020), this

82   process warrants investigation in human cells to complement mouse *in vivo* studies.

83   Prior studies have evaluated the impact of Wnt activation in immortalized human brain

84   ECs and observed only modest effects on barrier phenotype (Paolinelli et al., 2013; Laksitorini et

85   al., 2019). Combined with the aforementioned deficits observed in primary adult mouse brain

86   endothelial cells that are not rescued by ectopic Wnt activation (Sabbagh and Nathans, 2020),

87   one possibility is that mature, adult endothelium is largely refractory to Wnt activation, and that

88   Wnt responsiveness is a property of immature endothelial cells analogous to those in the

89   perineural vascular plexus. Human pluripotent stem cells (hPSCs) offer a potential human model

90   system for investigation of molecular mechanisms of BBB phenotype acquisition. However,

91   currently available hPSC-based models of CNS endothelial-like cells are not well suited for

4

92   modeling the BBB developmental progression as they do not follow a developmentally-relevant

93   differentiation trajectory, lack definitive endothelial identity, or have been incompletely

94   characterized with respect to the role of developmental signaling pathways (Lippmann et al.,

95   2020; Workman and Svendsen, 2020). As a potential alternative, hPSCs can also be used to

96   generate immature, naïve endothelial progenitors (Lian et al., 2014) that could be used to better

97   explore the induction of BBB phenotypes. For example, we recently reported that extended

98   culture of such hPSC-derived endothelial progenitors in a minimal medium yielded ECs with

99   improved BBB tight junction protein expression and localization which led to improved

100   paracellular barrier properties (Nishihara et al., 2020). However, as shown below, these cells

101   exhibit high expression of PLVAP and little expression of GLUT-1, indicating the need for

102   additional cues to drive CNS EC specification.

103   In this work, we tested the hypothesis that activation of Wnt/β-catenin signaling in hPSC-

104   derived, naïve endothelial progenitors would drive development of a CNS EC-like phenotype.

105   We found that many aspects of the CNS EC phenotype, including the canonical GLUT-1,

106   claudin-5, and PLVAP expression effects, were regulated by CHIR 99021, a small molecule

107   agonist of Wnt/β-catenin signaling. Wnt ligands and conditioned media from neural progenitors

108   produced a more limited response, as did CHIR treatment in matured ECs. Whole-transcriptome

109   analysis revealed definitive endothelial identity of the resulting cells and CHIR-upregulated

110   expression of known CNS EC transcripts, including *LEF1*, *APCDD1*, *AXIN2*, *SLC2A1*, *CLDN5*,

111   *LSR*, *ABCG2*, *SOX7*, and *ZIC3*. We also observed an unexpected CHIR-mediated upregulation of

112   caveolin-1, which did not, however, correlate with increased uptake of a dextran tracer. Thus, we

113   provide evidence that Wnt activation in hPSC-derived naïve endothelial progenitors is sufficient

114   to induce many aspects of the CNS barrier EC phenotype, and we establish a model system for

115   further systematic investigation of putative barriergenic cues.

5

RESULTS

Wnt activation in hPSC-derived endothelial progenitors

We adapted an existing protocol to produce endothelial progenitor cells (EPCs) from hPSCs (Lian et al., 2014; Bao et al., 2016) (Figure 1A). To achieve mesoderm specification, this method employs an initial activation of Wnt/β-catenin signaling with CHIR 99021 (CHIR), a small molecule inhibitor of glycogen synthase kinase-3 (GSK-3), which results in inhibition of GSK-3β-mediated β-catenin degradation. After 5 days of expansion, the resulting cultures contained a mixed population of $CD34^+CD31^+$ EPCs and $CD34^-CD31^-$ non-EPCs (Figure 1B-C). We used magnetic-activated cell sorting (MACS) to isolate $CD31^+$ cells from this mixed culture and plated these cells on collagen IV-coated plates in a minimal endothelial cell medium termed hECSR (Nishihara et al., 2020). We first asked whether Wnt3a, a ligand widely used to activate canonical Wnt/β-catenin signaling (Kim et al., 2005, 2008; Liebner et al., 2008; Cecchelli et al., 2014; Praça et al., 2019), could induce GLUT-1 expression in the resulting ECs. After 6 days of treatment, we observed a significant increase in the fraction of $GLUT-1^+$ ECs in Wnt3a-treated cultures compared to controls (Figure 1D-E). Consistent with previous observations (Nishihara et al., 2020), we also detected a population of $calponin^+$ smooth muscle protein $22-α^+$ putative smooth muscle-like cells (SMLCs) outside the endothelial colonies (Figure 1–figure supplement 1) and these SMLCs expressed GLUT-1 in both control and Wnt3a-treated conditions (Figure 1D).

Based on these promising results with Wnt3a, we next tested several additional strategies for Wnt activation and, in addition to GLUT-1, evaluated expression of two other key proteins: claudin-5, which is known to be upregulated in CNS ECs in response to Wnt (Benz et al., 2019), and caveolin-1, given the low rate of caveolin-mediated transcytosis in CNS compared to non-CNS ECs (Reese and Karnovsky, 1967; Andreone et al., 2017). First, we tested Wnt7a and

6

140   Wnt7b, the ligands primarily responsible for Wnt activation in CNS ECs *in vivo* (Daneman et al.,

141   2009; Cho et al., 2017). We also tested Wnt ligands in combination with R-spondin 1 (Rspo1), a

142   potentiator of Wnt signaling that inhibits the RNF43/ZNRF3-mediated negative feedback

143   mechanism by which Frizzled receptors are endocytosed (Kim et al., 2005, 2008; Koo et al.,

144   2012; Clevers et al., 2014). Finally, we tested a low concentration (4 µM) of the GSK-3 inhibitor

145   CHIR because of its ability to activate Wnt signaling in a receptor/co-receptor-independent

146   manner. We found that Wnt7a and the combination of Wnt7a and Wnt7b, but not Wnt7b alone,

147   slightly increased the fraction of GLUT-1$^+$ ECs, while Rspo1 did not affect EC purity or

148   expression of GLUT-1, claudin-5 or caveolin-1 (Figure 2A-C). Interestingly, Wnt7a, but not

149   Wnt3a, also increased the proportion of ECs compared to SMLCs (Figure 2A,C). By contrast, 4

150   µM CHIR robustly induced GLUT-1 expression in approximately 90% of ECs while increasing

151   EC purity to a level similar to that achieved with Wnt7a. Furthermore, CHIR led to an

152   approximately 1.5-fold increase in average claudin-5 abundance and a nearly 30-fold increase in

153   GLUT-1 abundance, but also a 4-fold increase in caveolin-1 (Figure 2A,C). We therefore titrated

154   CHIR to determine an optimal concentration for EC expansion, purity, GLUT-1 induction, and

155   claudin-5 upregulation while limiting the undesirable non-CNS-like increase in caveolin-1

156   abundance. Although 2 µM CHIR did not lead to increased caveolin-1 expression compared to

157   vehicle control (DMSO), it also did not elevate claudin-5 or GLUT-1 expression compared to

158   control and was less effective in increasing EC number and EC purity than 4 µM CHIR (Figure

159   2–figure supplement 1). On the other hand, 6 µM CHIR further increased GLUT-1 abundance

160   but also further increased caveolin-1 abundance and did not improve EC number, EC purity, or

161   claudin-5 expression (Figure 2–figure supplement 1). Therefore, we conducted further

162   experiments using 4 µM CHIR. We confirmed that the CHIR-mediated increases in EC purity,

163   EC number, and caveolin-1 and GLUT-1 expression were conserved in an additional hPSC line,

7

164 although claudin-5 upregulation was not apparent (Figure 2–figure supplement 2). We also used

165 two hPSC lines with doxycycline-inducible expression of short hairpin RNAs targeting *CTNNB1*

166 (β-catenin) to confirm that CHIR-mediated upregulation of GLUT-1 in ECs was β-catenin-

167 dependent. Indeed, doxycycline treatment in combination with CHIR significantly reduced

168 GLUT-1 abundance in ECs derived from these hPSC lines (Figure 2–figure supplement 3).

169 Together, these results suggest that Wnt pathway activation, either with ligands or CHIR, is

170 capable of inducing CNS-like phenotypes in hPSC-derived endothelial progenitors.

171   In the CNS, neural progenitors and astrocytes are the primary sources of Wnt ligands

172 resulting in induction and maintenance of EC barrier properties. Because the relatively weak

173 response to Wnt ligands observed in our system is potentially attributable to poor potency

174 associated with the recombinant proteins, we reasoned that relevant cellular sources of Wnt

175 ligands might be more effective in activating Wnt in EPCs. To this end, we differentiated hPSCs

176 to neural rosettes, which are radially organized Pax6$^+$ neural progenitors, and astrocytes

177 according to established protocols (Ebert et al., 2013; Lippmann et al., 2014; Sareen et al., 2014;

178 Canfield et al., 2017). Importantly, RNA-seq data from the literature suggest that both hPSC-

179 derived neural rosettes and astrocytes express *WNT7A* (Vatine et al., 2016; Shang et al., 2018).

180 We collected neural rosette-conditioned medium (NR-CM) and astrocyte-conditioned medium

181 (Astro-CM) and treated EPCs with these media for 6 days. Similar to our observations with

182 Wnt7a, both NR-CM and Astro-CM significantly increased the proportion of ECs compared to

183 SMLCs (Figure 3A,C). NR-CM, but not Astro-CM, also induced weak GLUT-1 expression in

184 ECs, reminiscent of the Wnt7a-induced phenotype, although this induction was much weaker

185 than in the CHIR-treated cells (Figure 3B,D). NR-CM and Astro-CM had variable effects with

186 respect to caveolin-1 and claudin-5 expression (Figure 3D). In summary, NR-CM performed

187 similarly to Wnt7a in weakly inducing GLUT-1 expression and increasing EC purity. The

188 comparatively stronger response to CHIR may suggest either that the potency or concentration of

189 ligands is insufficient, or that the EPCs lack the full machinery of receptors and co-receptors

190 necessary to transduce the Wnt ligand signal (analyzed further below).

191

192 **Effects of CHIR-mediated Wnt activation in endothelial progenitors**

193 Since CHIR elicited the most robust Wnt-mediated response, we next asked whether

194 other aspects of the CNS EC barrier phenotype were CHIR-regulated. PLVAP, a protein that

195 forms bridges across both caveolae and fenestrae (Herrnberger et al., 2012), is one such

196 canonically Wnt-downregulated protein. We therefore first evaluated PLVAP expression in

197 Passage 1 control (DMSO) or CHIR-treated ECs using confocal microscopy (Figure 4A). We

198 observed numerous PLVAP$^+$ punctate vesicle-like structures in both conditions, with CHIR

199 treatment reducing PLVAP abundance by approximately 20% (Figure 4A-B). This effect was not

200 apparent in Western blots of Passage 1 ECs, likely due to the relatively modest effect (Figure

201 5A-B). However, after two more passages (Figure 1A), Passage 3 ECs demonstrated a robust

202 downregulation of PLVAP in CHIR-treated cells compared to controls (Figure 5C-D). We also

203 used Western blotting to confirm CHIR-mediated upregulation of GLUT-1 and claudin-5 both at

204 Passage 1 and Passage 3 (Figure 5A-D). We next evaluated expression of the tricellular tight

205 junction protein LSR (angulin-1) because of its enrichment in CNS versus non-CNS ECs, and

206 the temporal similarity between LSR induction and the early stage of Wnt-mediated CNS

207 barriergenesis (Sohet et al., 2015). We found that CHIR treatment led to a strong increase in LSR

208 expression in both Passage 1 and Passage 3 ECs (Figure 5A-D), suggesting that Wnt signaling

209 upregulates multiple necessary components of the CNS EC bicellular and tricellular junctions.

210 CHIR treatment produced two apparently competing changes in ECs related to vesicular

211 transport: an expected downregulation of PLVAP and an unexpected upregulation of caveolin-1.

9

212   We therefore asked whether the rate of total fluid-phase endocytosis differed between CHIR-

213   treated and control ECs, using a fluorescently-labeled 10 kDa dextran as a tracer. After

214   incubating Passage 1 cultures with dextran for 2 h at 37°C, we used flow cytometry to gate

215   CD31$^+$ ECs and assess total dextran accumulation (Figure 6A-B). We first confirmed that the

216   process of dextran internalization required the membrane fluidity of an endocytosis-dependent

217   process by carrying out the assay at 4°C; this condition indeed yielded a substantially decreased

218   dextran signal compared to 37°C (Figure 6B). In ECs incubated at 37°C, CHIR treatment did not

219   change the geometric mean dextran signal compared to DMSO (Figure 6B,C), but did cause a

220   broadening of the distribution of dextran intensities, indicative of sub-populations of cells with

221   decreased and increased dextran uptake (Figure 6B,D). Importantly, these results were consistent

222   across three independent differentiations (Figure 6C-D). Thus, despite the generally uniform

223   elevation of caveolin-1 and decrease of PLVAP observed by immunocytochemistry in CHIR-

224   treated ECs, our functional assay suggests neither an overall increase nor decrease in total fluid-

225   phase endocytosis. Instead, it indicates that CHIR increases the heterogeneity of the EC

226   population with respect to the rate of endocytosis.

227   Given the relatively weak responses to Wnt activation in adult mouse liver ECs *in vivo*

228   (Munji et al., 2019) and adult mouse brain ECs cultured *in vitro* (Sabbagh and Nathans, 2020),

229   we sought to determine whether the immature, potentially more plastic state of hPSC-derived

230   endothelial progenitors contributed to the relatively robust CHIR-mediated response we

231   observed. To test this hypothesis, we matured hPSC-derived ECs *in vitro* for 4 passages (until

232   approximately day 30) prior to initiating CHIR treatment for 6 days (Figure 7A). The resulting

233   Passage 5 DMSO-treated ECs, which are analogous to EECM-BMEC-like cells we previously

234   reported (Nishihara et al., 2020), did not have detectable GLUT-1 expression (Figure 7B).

235   Compared to DMSO controls, the resulting CHIR-treated Passage 5 ECs exhibited an

236   approximately 1.5-fold increase in GLUT-1 abundance (Figure 7B-C), a markedly weaker

237   response than the 10- to 40-fold increases routinely observed using the same

238   immunocytochemistry-based assay when CHIR treatment was initiated immediately after MACS

239   (Figure 2; Figure 2–figure supplement 1; Figure 2–figure supplement 2; Figure 3). Furthermore,

240   CHIR treatment in matured ECs led to a slight decrease in EC number (Figure 7D), rather than

241   the increase observed when treatment was initiated immediately after MACS (Figure 2–figure

242   supplement 1; Figure 3). Together, these data suggest that early, naïve endothelial progenitors

243   are more responsive to Wnt activation than more mature ECs derived by the same differentiation

244   protocol.

245

Comprehensive profiling of the Wnt-regulated endothelial transcriptome

247   We turned next to RNA-sequencing as an unbiased method to assess the impacts of Wnt

248   activation on the EC transcriptome. We performed four independent differentiations and

249   analyzed Passage 1 ECs treated with DMSO, CHIR, or Wnt7a and Wnt7b (Wnt7a/b), using

250   fluorescence-activated cell sorting (FACS) to isolate CD31$^+$ ECs from the mixed EC/SMLC

251   cultures. We also sequenced the SMLCs from DMSO-treated cultures at Passage 1 from two of

252   these differentiations. DMSO- and CHIR-treated ECs at Passage 3 from three of these

253   differentiations were also sequenced. Principal component analysis of the resulting whole-

254   transcriptome profiles revealed that the two cell types (ECs and SMLCs) segregated along

255   principal component (PC) 1, which explained 52% of the variance. In ECs, the effects of passage

256   number and treatment were reflected in PC 2, which explained 20% of the variance (Figure 8A).

257   We next validated the endothelial identity of our cells; we observed that canonical endothelial

258   marker genes (including *CDH5, CD34, PECAM1, CLDN5, ERG,* and *FLI1*) were enriched in

259   ECs compared to SMLCs and had high absolute abundance, on the order of 100–1,000

11

260   transcripts per million (TPM) (Figure 8B; Supplementary file 1). SMLCs expressed

261   mesenchymal (mural/fibroblast)-related transcripts (including *PDGFRB, CSPG4, PDGFRA,*

262   *TBX2, CNN1,* and *COL1A1*), which ECs generally lacked, although we did observe slight

263   enrichment of some of these genes in Passage 1 DMSO-treated ECs, likely reflective of a small

264   amount of SMLC contamination despite CD31 FACS (Figure 8B). SMLCs also expressed

265   *SLC2A1* (Supplementary file 1) consistent with protein-level observations (Figure 1D). We also

266   observed little to no expression of the epithelial genes *CDH1, EPCAM, CLDN1, CLDN3* (Castro

267   Dias et al., 2019), *CLDN4,* and *CLDN6,* reflecting the definitive endothelial nature of the cells

268   (Figure 8B; Supplementary file 1).

269   First comparing CHIR- and DMSO-treated ECs at Passage 1, we identified 1,369

270   significantly upregulated genes and 2,037 significantly downregulated genes (Figure 8C;

271   Supplementary file 2). CHIR-upregulated genes included *SLC2A1, CLDN5, LSR,* and *CAV1,*

272   consistent with protein-level assays. *PLVAP* was downregulated, as were a number of

273   mesenchymal genes (*TAGLN, COL1A1*), again reflective of slight contamination of SMLC

274   transcripts in the DMSO-treated EC samples (Figure 8C-D). Additionally, important downstream

275   effectors of Wnt signaling were upregulated, including the transcription factors *LEF1* and *TCF7* ,

276   the negative regulator *AXIN2*, and the negative regulator *APCDD1*, which is known to modulate

277   Wnt-regulated barriergenesis in retinal endothelium (Mazzoni et al., 2017) (Figure 8C-D). We

278   also found that the transcription factors *ZIC3,* which is highly enriched in brain and retinal ECs

279   *in vivo* and downstream of Frizzled4 signaling (Wang et al., 2012; Sabbagh et al., 2018), and

280   *SOX7*, which acts cooperatively with *SOX17* and *SOX18* in retinal angiogenesis (Zhou et al.,

281   2015), were upregulated by CHIR in our system (Figure 8D). Additional CHIR-upregulated

282   genes included *ABCG2* (encoding the efflux transporter Breast Cancer Resistance Protein,

283   BCRP), and *APLN*, a tip cell marker enriched in postnatal day 7 murine brain ECs compared to

284   those of other organs, and subsequently downregulated in adulthood (Sabbagh et al., 2018;

285   Sabbagh and Nathans, 2020) (Figure 8C). Finally, we detected CHIR-mediated downregulation

286   of the fatty acid-binding protein-encoding *FABP4*, which is depleted in brain ECs compared to

287   those of peripheral organs (Sabbagh et al., 2018). We also observed similar downregulation of

288   *SMAD6*, which is depleted in brain ECs compared to lung ECs and is a putative negative

289   regulator of BMP-mediated angiogenesis (Mouillesseaux et al., 2016; Vanlandewijck et al.,

290   2018) (Figure 8D). Many of these CHIR-mediated gene expression changes persisted at Passage

291   3, including *SLC2A1*, *LSR*, *LEF1*, *AXIN2*, *APCDD1*, *ZIC3*, and *ABCG2* upregulation and *PLVAP*

292   downregulation (Figure 8E; Figure 8–figure supplement 1A).

293   We made similar comparisons (i) between Wnt7a/b-treated and control (DMSO-treated)

294   ECs at Passage 1, and (ii) between control ECs at Passage 3 versus Passage 1 (Figure 8E; Figure

295   8–figure supplement 1B-C; Supplementary file 2). Consistent with the weak response observed

296   by immunocytochemistry, there were fewer Wnt7a/b-mediated gene expression changes

297   compared to those elicited by CHIR, with 241 upregulated and 420 downregulated genes (Figure

298   8–figure supplement 1B). In general, however, these changes were consistent with CHIR-

299   mediated changes, with 104 concordantly upregulated genes, 302 concordantly downregulated

300   genes, and only 23 discordantly regulated genes (Figure 8E). Of note, treatment with Wnt7a/b,

301   but not CHIR, upregulated *SOX17*, a Wnt target gene required for BBB function (Corada et al.,

302   2018). Extended culture to Passage 3 in the absence of exogenous Wnt activation led to 1,521

303   upregulated genes, including *CLDN5* and *CAV1*, consistent with previously-reported protein-

304   level observations in EECM-BMEC-like cells (Nishihara et al., 2020), which are analogous to

305   Passage 3 DMSO-treated cells. We also observed 1,625 downregulated genes, including *PLVAP*

306   (Figure 8–figure supplement 1C). *SLC2A1,* however, was not upregulated at Passage 3 (Figure

307   8–figure supplement 1C), concordant with absence of GLUT-1 protein expression in the control

13

308   ECs (Figure 7B). To further understand the strengths and limitations of this model system both

309   as a readout of early developmental changes in CNS ECs (Passage 1 cells) or as a source of

310   CNS-like ECs for use in downstream modeling applications, we evaluated absolute transcript

311   abundance and effects of treatment or passage number on 53 characteristic CNS EC genes

312   encompassing tight junction components, vesicle trafficking machinery, solute carriers, and

313   ATP-binding cassette (ABC) efflux transporters selected based on high expression in human

314   brain endothelial cells from a meta-analysis of single cell RNA-seq data (Gastfriend et al., 2021)

315   (Figure 8–figure supplement 1D). While ECs expressed *CLDN5*, *TJP1*, *TJP2*, *OLCN*, and *LSR*,

316   they lacked *MARVELD2* (encoding tricellulin) under all conditions. ECs under all conditions

317   also lacked *MFSD2A* and, despite CHIR-mediated downregulation of *PLVAP*, retained high

318   absolute expression of this and other caveolae-associated genes. Finally, while many solute

319   carriers and ABC transporters were expressed (*SLC2A1*, *SLC3A2*, *SLC16A1*, *SLC38A2*, *ABCG2*),

320   others expressed at the *in vivo* human BBB were not (*SLC5A3*, *SLC7A11*, *SLC38A3*, *SLCO1A2*,

321   *ABCB1*) (Figure 8–figure supplement 1D). Thus, while CHIR treatment yields ECs with certain

322   elements of CNS-like character, additional molecular signals are likely necessary to improve

323   other aspects of the *in vivo* CNS EC phenotype.

324   To partially address the hypothesis that the weak response of ECs to Wnt7a/b, NR-CM,

325   and Astro-CM is due to a lack of necessary Wnt receptors and/or co-receptors, we used RNA-seq

326   data from Passage 1 DMSO-treated ECs to evaluate expression of transcripts encoding these and

327   other components of the canonical Wnt signaling pathway. *FZD4* and *FZD6* were highly

328   expressed and enriched compared to all other Frizzleds (Figure 8–figure supplement 2),

329   consistent with data from murine brain ECs *in vivo* (Daneman et al., 2009). *RECK* and *ADGRA2*

330   (*GPR124*) were moderately expressed at a level similar to *LRP6* (on the order of 40 TPM), while

331   little to no *LRP5* was expressed (Figure 8–figure supplement 2). Taken together, however, these

332   data suggest that the hPSC-derived ECs express much of the machinery necessary to transduce

333   the signal from Wnt7a/b ligands, but possibilities remain that the proteins encoded by the

334   evaluated transcripts are absent, or at too low an abundance, for a robust response, motivating the

335   use of CHIR to bypass the cell surface Wnt pathway components for robust induction of

336   barriergenesis via β-catenin stabilization.

337

338   **The Wnt-regulated endothelial transcriptome in multiple contexts**

339   To globally assess whether CHIR-mediated gene expression changes in our system are

340   characteristic of the responses observed in ECs *in vivo* and similar to those observed in other *in*

341   *vitro* contexts, we compared our RNA-seq dataset to those of studies that employed a genetic

342   strategy for β-catenin stabilization (the *Ctnnb1*^{flex3} allele) in adult mouse ECs in several contexts:

343   (i) pituitary ECs, which acquire some BBB-like properties upon β-catenin stabilization (Wang et

344   al., 2019); (ii) liver ECs, which exhibit little to no barriergenic response to β-catenin stabilization

345   (Munji et al., 2019); (iii) brain ECs briefly cultured *in vitro*, which rapidly lose their BBB-

346   specific gene expression profile even with β-catenin stabilization (Sabbagh and Nathans, 2020),

347   and offer the most direct comparison to our *in vitro* model system. Upon recombination, the

348   *Ctnnb1*^{flex3} allele produces a dominant mutant β-catenin lacking residues that are phosphorylated

349   by GSK-3β to target β-catenin for degradation (Harada et al., 1999); as such, this strategy for

350   ligand- and receptor-independent Wnt activation by β-catenin stabilization is directly analogous

351   to CHIR treatment.

352   We first used literature RNA-seq data from postnatal day 7 murine brain, liver, lung, and

353   kidney ECs (Sabbagh et al., 2018) to define core sets of genes in brain ECs that are differentially

354   expressed compared to all three of the other organs (Figure 9A-B). Using the resulting sets of

355   1094 brain-enriched and 506 brain-depleted genes, we asked how many genes in our Passage 1

15

356 ECs were concordantly-regulated by CHIR: 130 of the brain-enriched genes were CHIR-

357 upregulated and 116 of the brain-depleted genes were CHIR-downregulated (Figure 9C). In

358 pituitary ECs with β-catenin stabilization, 102 of the brain enriched genes were upregulated with

359 and 48 of the brain depleted genes were downregulated (Figure 9D). Compared with the pituitary

360 ECs, there were far fewer concordantly-regulated genes in liver ECs with β-catenin stabilization,

361 with 25 upregulated and 1 downregulated (Figure 9E). Finally, cultured primary mouse brain

362 ECs with β-catenin stabilization exhibited 72 upregulated and 16 downregulated genes (Figure

363 9F). The only gene concordantly-regulated in all four comparisons was the canonical Wnt target

364 *AXIN2*. Several additional genes were concordantly upregulated in three of four, including

365 *TCF7*, *FAM107A*, *NKD1*, *TNFRSF19*, *GLUL*, *SLC30A1*, and *ABCB1*, which was the only gene

366 concordantly regulated in all comparisons except the hPSC-derived ECs (Figure 9G). Several

367 canonical target genes were shared by the hPSC-derived EC and pituitary EC systems, including

368 *APCDD1*, *LEF1*, *CLDN5*, and *SLC2A1*; also in this category were *LSR*, the zinc/manganese

369 transporter *SLC39A8*, and 12 additional genes (Figure 9G). Notably, the caveolae inhibitor

370 *MFSD2A* was robustly upregulated by β-catenin in pituitary ECs, but not in any other context

371 (Figure 9C-F), suggesting other brain-derived factors may cooperate with Wnt to regulate

372 expression of this important inhibitor of caveolin-mediated transcytosis. Complete gene lists

373 from this comparative analysis are provided in Supplementary file 3. In sum, the data suggest

374 that the hPSC-derived ECs responded to Wnt activation in a fashion that led to modest induction

375 of CNS transcriptional programs and that the response was most similar to the pituitary β-catenin

376 stabilization model. Importantly, this analysis also supports the hypothesis that immature

377 endothelium is highly responsive to Wnt activation where mature (adult) endothelium is largely

378 refractory except in regions proximal to barrier-forming regions.

16

DISCUSSION

The Wnt/β-catenin signaling pathway plays a central role in CNS angiogenesis and in establishing the unique properties of CNS ECs (Liebner et al., 2008; Stenman et al., 2008; Daneman et al., 2009; Kuhnert et al., 2010; Cullen et al., 2011; Vanhollebeke et al., 2015; Cho et al., 2017). In this work, we investigated the role of Wnt/β-catenin signaling on induction of BBB properties in a human EC model, using naïve endothelial progenitors derived from hPSCs. We reasoned that these immature EPCs (Lian et al., 2014) would be similar to the immature endothelium in the perineural vascular plexus and thus competent to acquire CNS EC phenotypes in response to Wnt activation. We evaluated several strategies to activate Wnt, including the widely used ligand Wnt3a (Liebner et al., 2008), the neural progenitor- and astrocyte-derived ligands Wnt7a and Wnt7b, which are the two Wnt ligands primarily responsible for the Wnt-dependent effects of CNS angiogenesis and barriergenesis observed *in vivo* (Daneman et al., 2009; Cho et al., 2017), neural rosette- and astrocyte-CM as putative cellular sources of Wnt ligands, and the GSK-3 inhibitor CHIR.

We found that CHIR treatment robustly induced several canonical CNS EC molecular phenotypes, including a marked induction of GLUT-1, upregulation of claudin-5, and downregulation of PLVAP, which correlated with differential gene expression in RNA-seq data. Further, using RNA-seq and Western blotting, we also identified LSR (angulin-1) as CHIR-induced in this system, supporting the notion that this highly CNS EC-enriched tricellular tight junction protein (Daneman et al., 2010a; Sohet et al., 2015) is Wnt-regulated. In RNA-seq data, we observed differential expression of known CNS EC-enriched/depleted and Wnt-regulated genes including upregulated *LEF1*, *AXIN2*, *APCDD1*, *ABCG2*, *SOX7*, and *ZIC3* and downregulated *PLVAP*, *FABP4*, and *SMAD6*. These RNA-seq data should therefore be useful in generating hypotheses of BBB-associated genes regulated by Wnt activation in ECs, for future

403   functional studies. Our work also defines an important set of phenotypes for which Wnt

404   activation in ECs is not sufficient in our system: in the context of vesicle trafficking, we

405   observed caveolin-1 (*CAV1*) upregulation, no change in mean functional endocytosis, virtually

406   no expression of *MFSD2A*, and high absolute *PLVAP* abundance despite CHIR-mediated

407   downregulation. Given roles of brain pericytes in regulating PLVAP, MFSD2A, and functional

408   transcytosis (Armulik et al., 2010; Daneman et al., 2010b; Ben-Zvi et al., 2014; Stebbins et al.,

409   2019), and the observation that MFSD2A is Wnt-regulated in pituitary ECs *in vivo* (Wang et al.,

410   2019), where pericytes are present, it is plausible that pericyte-derived cues are necessary in

411   addition to Wnts to achieve the characteristically low rate of CNS EC pinocytosis. Next, while

412   *ABCG2* (BCRP) was Wnt-induced in our system, other hallmark efflux transporters were not

413   Wnt-regulated and either expressed at low levels (e.g., *ABCC4*, encoding MRP-4) or not

414   expressed (e.g. *ABCB1*, encoding P-glycoprotein). Notably however, *Abcb1a* was Wnt-regulated

415   in the three other β-catenin stabilization experiments from the literature that we evaluated (Munji

416   et al., 2019; Wang et al., 2019; Sabbagh and Nathans, 2020). Thus, pericyte-derived cues,

417   astrocyte-derived cues, and/or activation of the pregnane X or other nuclear receptors may be

418   important for complete acquisition of the complement of CNS EC efflux transporters (Bauer et

419   al., 2004; Berezowski et al., 2004; Praça et al., 2019).

420   While several recombinant Wnt ligands and neural rosette-CM elevated GLUT-1

421   expression in ECs, the magnitude of this effect was small compared to the robust induction of

422   GLUT-1 observed with CHIR treatment. While we observed moderate transcript-level

423   expression *RECK* and *ADGRA2* (*GPR124*) in Passage 1 ECs, it is possible that protein-level

424   expression of these necessary Wnt7 coreceptors, or additional components necessary for Wnt

425   signal transduction, are not of sufficient abundance. For example, absence of LRP5 is a potential

426   factor in the muted response to Wnt ligands and CM because LRP5 and LRP6 likely have non-

427 redundant functions, as evidenced by defects in retinal barrier formation in *Lrp5*-knockout mice

428 (Zhou et al., 2014). Presence of GPR124 in naïve endothelial progenitors is consistent with

429 ubiquitous expression in ECs in the mouse embryo that is subsequently downregulated in non-

430 CNS endothelium; however, GPR124 enrichment in CNS ECs can be observed as early as E12.5

431 (Kuhnert et al., 2010), leaving open the possibility that during development other neural tissue-

432 derived signals upregulate or maintain RECK and GPR124 expression. Furthermore, while

433 ligand potency or concentration may also play a role in the weak response, we observed a

434 consistent and highly potent EC-purifying effect (i.e., reduction or elimination of the

435 contaminating SMLCs observed in control Passage 1 cultures) with Wnt7a and both neural

436 rosette- and astrocyte-CM. CHIR also achieved this purifying effect and increased EC number,

437 suggesting that Wnt signaling plays a role in suppressing proliferation of mesoderm-derived

438 mural cells in this system.

439   We also directly addressed the hypothesis that immature ECs are more plastic, that is,

440 more competent to acquire BBB properties upon Wnt activation, than mature ECs. This

441 hypothesis is supported by existing observations that ectopic expression of Wnt7a is sufficient to

442 induce GLUT-1 expression in non-CNS regions of the mouse embryo (Stenman et al., 2008), but

443 β-catenin stabilization in adult mouse liver and lung ECs produces only a slight effect (Munji et

444 al., 2019). We repeated our CHIR treatment paradigm in hPSC-derived ECs after an extended

445 period of *in vitro* culture, and observed much weaker induction of GLUT-1 and no pro-

446 proliferative effect. Thus, our results support this hypothesis and suggest that the loss of BBB

447 developmental plasticity in ECs is an intrinsic, temporally-controlled process rather than a result

448 of the peripheral organ environment. Interestingly, ECs in non-BBB-forming regions of the CNS

449 (i.e., CVOs), and in the anterior pituitary, which is directly proximal to the CNS, retain some of

450 their plasticity in adulthood (Wang et al., 2019), possibly as the result of a delicate balance

19

451   between Wnt ligands and Wnt-inhibitory factors in these regions. Our model should facilitate

452   additional systematic examination of factors that may enhance or attenuate EC Wnt

453   responsiveness.

454   Finally, our work establishes an improved hPSC-based model for investigating

455   mechanisms of BBB development in naïve ECs. hPSCs are an attractive model system to

456   complement *in vivo* animal studies because they (i) are human, (ii) permit investigation of

457   developmental processes in contrast to primary or immortalized cells, (iii) are highly scalable,

458   (iv) can be derived from patients to facilitate disease modeling and autologous coculture systems,

459   and (v) are genetically tractable. While widely used hPSC-based BBB models are useful for

460   measuring molecular permeabilities and have been employed to understand genetic contributions

461   to barrier dysfunction (Vatine et al., 2016, 2019; Lim et al., 2017), they have not been shown to

462   proceed through a definitive endothelial progenitor intermediate (Lippmann et al., 2012; Lu et

463   al., 2021) and express epithelial-associated genes (Qian et al., 2017; Delsing et al., 2018; Vatine

464   et al., 2019; Lu et al., 2021). Thus, new models with developmentally relevant differentiation

465   trajectories and definitive endothelial phenotype are needed for improved understanding of

466   developmental mechanisms. Motivated in part by prior use of endothelial cells derived from

467   hematopoietic progenitors in human cord blood to generate BBB models (Boyer-Di Ponio et al.,

468   2014; Cecchelli et al., 2014), we and others recently showed that hPSC-derived naïve endothelial

469   progenitors or ECs are good candidates for such a system (Praça et al., 2019; Nishihara et al.,

470   2020; Roudnicky et al., 2020a, 2020b). For example, Praça *et al.* showed that a combination of

471   VEGF, Wnt3a, and retinoic acid directed EPCs to brain capillary-like ECs with moderate

472   transendothelial electrical resistance (TEER) of $\sim 60 \times cm^2$. We previously showed that BBB-like

473   paracellular barrier characteristics are induced in hPSC-EPC-derived ECs after extended culture

474   in a minimal medium. These so-called EECM-BMEC-like cells had TEER and small molecule

475 permeability similar to primary human brain ECs, well-developed tight junctions, and an

476 immune cell adhesion molecule profile similar to brain ECs *in vivo* (Nishihara et al., 2020). In

477 this study, we showed it was possible to use the small molecule Wnt agonist CHIR to induce

478 additional hallmarks of CNS EC phenotype in hPSC-EPC-derived ECs, including canonical

479 GLUT-1, claudin-5, and PLVAP effects (both Passage 1 and 3 CHIR-treated ECs). However, it

480 is important to note that despite the improvements in CNS EC character with CHIR treatment,

481 further improvements to functional endocytosis, and efflux transporter and solute carrier

482 phenotype should be targets of future study and may be facilitated by cocultures and/or

483 additional molecular factors. Along these lines, the Passage 1 CHIR-treated CNS-like ECs would

484 be at a differentiation stage well suited to investigate cues subsequent to Wnt signaling that may

485 be key for the induction of additional CNS EC properties. Alternatively, the Passage 3 CHIR-

486 treated CNS-like ECs may be suitable for other BBB modeling applications. In summary, our

487 work has defined the EC response to Wnt activation in a simplified, human system and

488 established a new hPSC-derived *in vitro* model that will facilitate improved understanding of

489 endothelial barriergenesis.

21

MATERIALS AND METHODS

Key resources table

Reagent type	Designation	Source or reference	Identifier	Additional information
Cell line	iPSC: IMR90-4	Available from WiCell; (Jaffe et al., 2008)	RRID: CVCL_C437	
Cell line	iPSC: WTC11	Available from Gladstone Institutes; (Kreitzer et al., 2013)	RRID: CVCL_Y803	
Cell line	iPSC: CS03iCTRn2	Available from Cedars Sinai iPSC Core		
Cell line	iPSC: 19-9-11-7TGP-ishcat3	Laboratory stock		
Cell line	hESC: H9-7TGP-ishcat2	Laboratory stock (Lian et al., 2013)		
Cell line	hESC: H9-CDH5-eGFP	Laboratory stock (Bao et al., 2017)		
Cell line	Primary human brain vascular pericytes	ScienCell	1200	
Antibody	Anti-CD31-FITC (mouse IgG1, clone AC128)	Miltenyi Biotec	130-117-390	
Antibody	Anti-CD31-APC (mouse IgG1, clone AC128)	Miltenyi Biotec	130-119-891	
Antibody	Anti-CD34-FITC (mouse IgG2a, clone AC136)	Miltenyi Biotec	130-113-178	
Antibody	Anti-β-catenin-Alexa Fluor 488 (mouse IgG1, clone 14)	BD Biosciences	562505	1:100 (ICC)
Antibody	Anti-GLUT-1 (mouse IgG1, clone SPM498)	Invitrogen	MA5-11315	1:100 (ICC) 1:500 (WB)
Antibody	Anti-calponin (mouse IgG1, clone hCP)	Sigma-Aldrich	C2687	1:15000 (ICC)
Antibody	Anti-SM22α (rabbit polyclonal)	Abcam	ab10146	1:1000 (ICC)
Antibody	Anti-claudin-5 (mouse IgG1, clone 4C3C2)	Invitrogen	35-2500	1:100 (ICC) 1:500 (WB)
Antibody	Anti-caveolin-1 (rabbit polyclonal)	Cell Signaling Technology	3238	1:500 (ICC)
Antibody	Anti-VE-cadherin (mouse IgG2a, clone BV9)	Santa Cruz Biotechnology	sc-52751	1:100 (ICC) 1:250 (WB)
Antibody	Anti-β-actin (rabbit IgG, clone 13E5)	Cell Signaling Technology	4970	1:1000 (WB)
Antibody	Anti-PLVAP (rabbit polyclonal)	Prestige Antibodies	HPA002279	1:200 (ICC) 1:250 (WB)
Antibody	Anti-LSR (rabbit polyclonal)	Prestige Antibodies	HPA007270	1:250 (WB)
Antibody	Alexa Fluor 488 goat anti-mouse IgG	Invitrogen	A-11001	1:200 (ICC)
Antibody	Alexa Fluor 647 goat anti-rabbit IgG	Invitrogen	A-21245	1:200 (ICC)
Antibody	Alexa Fluor 488 goat anti-mouse IgG1	Invitrogen	A-21121	1:200 (ICC)
Antibody	Alexa Fluor 647 goat anti-mouse IgG2a	Invitrogen	A-21241	1:200 (ICC)
Antibody	Alexa Fluor 555 goat anti-rabbit IgG	Invitrogen	A-21428	1:200 (ICC)
Antibody	IRDye 800CW goat anti-mouse IgG	LI-COR Biosciences	926-32210	1:5000 (WB)
Antibody	IRDye 800CW goat anti-rabbit IgG	LI-COR Biosciences	926-32211	1:5000 (WB)
Antibody	IRDye 680RD goat anti-rabbit IgG	LI-COR Biosciences	926-68071	1:5000 (WB)
Commercial assay or kit	RNeasy Plus Micro Kit	Qiagen	74034	
Chemical compound or drug	CHIR 99021	Tocris	4423	
Chemical compound or drug	Dextran, Alexa Fluor 488; 10,000 MW, Anionic, Fixable	Invitrogen	D22910	

22

Software or algorithm	RSEM	(Li and Dewey, 2011)	v1.3.3
Software or algorithm	Bowtie2	(Langmead and Salzberg, 2012)	v2.4.2
Software or algorithm	R	R Foundation	v3.6.3
Software or algorithm	DESeq2	(Love et al., 2014)	v1.26.0
Software or algorithm	biomaRt	(Durinck et al., 2009)	v2.42.1
Software or algorithm	FIJI/ImageJ	(Schindelin et al., 2019)	v2.0.0-rc-68
Software or algorithm	Image Studio	LI-COR Biosciences	v5.2
Software or algorithm	FlowJo	BD Biosciences	v10.7.1
Software or algorithm	JMP Pro	SAS Institute	v14.0.0
Software or algorithm	Prism	GraphPad Software	v5.0.1

492

hPSC maintenance

Tissue culture plates were coated with Matrigel, Growth Factor Reduced (Corning, Glendale, AZ). A 2.5 mg aliquot of Matrigel was thawed and resuspended in 30 mL DMEM/F-12 (Life Technologies, Carlsbad, CA), and the resulting solution used to coat plates at 8.7 µg/cm^2 (1 mL per well for 6-well plates; 0.5 mL per well for 12-well plates). Plates were incubated at 37°C for at least 1 h prior to use. hPSCs were maintained on Matrigel-coated plates in E8 medium (STEMCELL Technologies, Vancouver, Canada) at 37°C, 5% CO_2. hPSC lines used were: IMR90-4 iPSC, WTC11 iPSC, CS03iCTRn2 iPSC, H9-CDH5-eGFP hESC, H9-7TGP-ishcat2 hESC, and 19-9-11-7TGP-ishcat3 iPSC. Medium was changed daily. When hPSC colonies began to touch, typically at approximately 70–80% confluence, cells were passaged using Versene (Life Technologies). Briefly, cells were washed once with Versene, then incubated with Versene for 7 min at 37°C. Versene was removed and cells were dissociated into colonies by gentle spraying with E8 medium. Cells were transferred at a split ratio of 1:12 to a new Matrigel-coated plate containing E8 medium.

23

Endothelial progenitor cell differentiation

EPCs were differentiated according previously published protocols (Lian et al., 2014; Bao et al., 2016; Nishihara et al., 2020) with slight modifications. On day -3 (D-3), hPSCs were treated with Accutase (Innovative Cell Technologies, San Diego, CA) for 7 min at 37°C. The resulting single cell suspension was transferred to 4× volume of DMEM/F-12 (Life Technologies) and centrifuged for 5 min, 200×g. Cell number was quantified using a hemocytometer. Cells were resuspended in E8 medium supplemented with 10 μM ROCK inhibitor Y-27632 dihydrochloride (Tocris, Bristol, United Kingdom) and seeded on Matrigel-coated 12-well plates at a density of $(1.5–2.5)\times10^4$ cells/cm^2, 1 mL per well. Cells were maintained at 37°C, 5% CO$_2$. On the following two days (D-2 and D-1), the medium was replaced with E8 medium. The following day (D0), differentiation was initiated by changing the medium to LaSR medium (Advanced DMEM/F-12 [Life Technologies], 2.5 mM GlutaMAX [Life Technologies], and 60 μg/ml L-ascorbic acid 2-phosphate magnesium [Sigma-Aldrich, St. Louis, MO]) supplemented with 7–8 μM CHIR 99021 (Tocris), 2 mL per well. The following day (D1), medium was replaced with LaSR medium supplemented with 7–8 μM CHIR 99021, 2 mL per well. On the following three days (D2, D3, and D4), the medium was replaced with pre-warmed LaSR medium (without CHIR), 2 mL per well.

On D5, EPCs were isolated using CD31 magnetic activated cell sorting (MACS). Cells were treated with Accutase for 15–20 min at 37°C. The resulting cell suspension was passed through a 40 μm cell strainer into an equal volume of DMEM (Life Technologies) supplemented with 10% FBS (Peak Serum, Wellington, CO) and centrifuged for 5 min, 200×g. Cell number was quantified using a hemocytometer. Cells were resuspended in MACS buffer (Dulbecco's phosphate buffered saline without Ca and Mg [DPBS; Life Technologies] supplemented with 0.5% bovine serum albumin [Sigma-Aldrich] and 2 mM EDTA [Sigma-Aldrich]) at a

24

531 concentration of 10^7 cells per 100 µL. The CD31-FITC antibody (Miltenyi Biotec, Auburn, CA)

532 was added to the cell suspension at a dilution of 1:50. The cell suspension was incubated for 30

533 min at room temperature, protected from light. The cell suspension was brought to a volume of

534 15 mL with MACS buffer and centrifuged for 5 min, 200×g. The supernatant was aspirated and

535 the pellet resuspended in MACS buffer at a concentration of 10^7 cells per 100 µL. The FITC

536 Selection Cocktail from the EasySep Human FITC Positive Selection Kit (STEMCELL

537 Technologies) was added at a dilution of 1:10 and the cell suspension was incubated for 20 min

538 at room temperature, protected from light. The Dextran RapidSpheres (magnetic particles)

539 solution from the Selection Kit was added at a dilution of 1:20 and the cell suspension was

540 incubated for an additional 15 min at room temperature.

541 The cell suspension was brought to a total volume of 2.5 mL with MACS buffer (for total

542 cell number less than 2×10^8, the approximate maximum yield from two 12-well plates; for a

543 larger number of plates/cells, a total volume of 5 mL was used). 2.5 mL of cell suspension was

544 transferred to a sterile 5 mL round-bottom flow cytometry tube and placed in the EasySep

545 magnet (STEMCELL Technologies) for 5 min. The magnet was inverted to pour off the

546 supernatant, the flow tube removed, the retained cells resuspended in 2.5 mL of MACS buffer,

547 and the flow tube placed back in the magnet for 5 min. This step was repeated 3 times, and the

548 resulting cell suspension transferred to a centrifuge tube, and centrifuged for 5 min, 200×g. Cell

549 number was quantified using a hemocytometer. Resulting EPCs were used directly for

550 experiments as described below or cryopreserved in hECSR medium supplemented with 30%

551 FBS and 10% DMSO for later use. hESCR medium is Human endothelial serum-free medium

552 (Life Technologies) supplemented with 1× B-27 supplement (Life Technologies) and 20 ng/mL

553 FGF2 (Waisman Biomanufacturing, Madison, WI).

Neural rosette differentiation

554

555   Neural rosettes were differentiated according to a previously published protocol

556   (Lippmann et al., 2014) with slight modifications. On D-1, IMR90-4 hPSCs were dissociated

557   with Accutase and seeded on Matrigel-coated plates in E8 medium supplemented with ROCK

558   inhibitor as described above, except the cell seeding density was 5×10^5 cells/cm². The following

559   day (D0), medium was replaced with E6 medium (DMEM/F-12 supplemented with 64 mg/L L-

560   ascorbic acid 2-phosphate magnesium, 14 µg/L sodium selenium, 543 mg/L sodium bicarbonate,

561   19.4 mg/L insulin [Roche, Penzberg, Germany], and 10.7 mg/L holo-transferrin [Sigma-

562   Aldrich]) prepared according to (Chen et al., 2011). Medium was replaced daily with E6 medium

563   on D1 through D5. On D6, medium was replaced with hECSR medium lacking FGF2. The

564   following day (D7), the resulting neural rosette-conditioned medium (NR-CM) was harvested

565   and stored at 4°C, and fresh hECSR medium lacking FGF2 was replaced. NR-CM was likewise

566   harvested on D8, D9, and D10. The resulting NR-CM aliquots were pooled, passed through a 0.2

567   µm filter, supplemented with 20 ng/mL FGF2, and used for experiments as described below.

Astrocyte differentiation

568

569   Astrocytes were differentiated via an hPSC-derived EZ sphere intermediate according to

570   previously published protocols (Ebert et al., 2013; Sareen et al., 2014; Canfield et al., 2017).

571   Briefly, CS03iCTRn2 hPSCs were dissociated with Versene and colonies were transferred to an

572   ultra-low attachment T-25 flask containing EZ sphere culture medium (a mixture of DMEM and

573   F-12 medium in a 7:3 ratio supplemented with 1× B-27 supplement minus vitamin A [Life

574   Technologies], 2 µg/mL heparin [Sigma-Aldrich], 100 ng/mL EGF [Peprotech], 100 ng/mL

575   FGF2, and 1× antibiotic-antimycotic [Life Technologies]). Half of the volume of EZ sphere

576   culture medium was replaced on Mondays, Wednesdays, and Fridays. EZ spheres were passaged

577   every Friday by mechanical dissociation with 2–4 passes on a McIlwain Tissue Chopper

26

578   (Campden Instruments, Loughborough, United Kingdom), with half of the resulting aggregates

579   returned to the flask and half discarded. To convert EZ spheres into astrospheres, which are

580   neural stem cell aggregates with enhanced astrocyte differentiation potential, medium was

581   changed to DMEM/F-12 supplemented with $1\times$ N-2 supplement (Life Technologies), 2 µg/mL

582   heparin, $1\times$ MEM-non-essential amino acids solution (Life Technologies), and 0.5 µM all-trans

583   retinoic acid (Sigma-Aldrich) and replaced daily for 11 days. The resulting spheres were

584   passaged as described above and returned to EZ sphere culture medium, which was replaced on

585   Mondays, Wednesdays, and Fridays. Astrospheres were passaged on Fridays as described above

586   and cultured for at least 30 passages prior to initiating astrocyte differentiation. To differentiate

587   astrocytes, astrospheres were treated with Accutase for 10–15 min at 37°C, followed by gentle

588   pipetting to dissociate and singularize the cells. The resulting single cell suspension was

589   transferred to $4\times$ volume of DMEM/F-12 and centrifuged for 5 min, 200×g. Cell number was

590   quantified using a hemocytometer. Cells were resuspended in EZ sphere culture medium and

591   seeded on Matrigel-coated plates at approximately 2.5×10^4 cells/cm^2. The following day,

592   medium was changed to astrocyte differentiation medium (DMEM/F-12 supplemented with $1\times$

593   N-2 supplement, 2 µg/mL heparin, and $1\times$ MEM-non-essential amino acids solution). This

594   medium was replaced every other day for 2 weeks. Medium was then replaced with hECSR

595   medium lacking FGF2. The following day, the resulting astrocyte-conditioned medium (Astro-

596   CM) was harvested and stored at 4°C, and fresh hECSR medium lacking FGF2 was replaced.

597   Astro-CM was likewise harvested on the following 3 days. The resulting Astro-CM aliquots

598   were pooled, passed through a 0.2 µm filter, supplemented with 20 ng/mL FGF2, and used for

599   experiments as described below.

27

Endothelial cell culture and treatment

Collagen IV (Sigma-Aldrich) was dissolved in 0.5 mg/mL acetic acid to a final concentration of 1 mg/mL. Collagen IV-coated plates were prepared by diluting a volume of this stock solution 1:100 in water, adding the resulting solution to tissue culture plates, or #1.5 glass bottom plates (Cellvis, Sunnyvale, CA) for cells intended for confocal imaging (1 mL per well for 6-well plates, 0.5 mL per well for 12-well plates, 0.25 mL per well for 24-well plates), and incubating the plates for 1 h at RT. Collagen IV coating solution was removed and EPCs obtained as described above were suspended in hECSR medium and plated at approximately 3×10^4 cells/cm^2. In some experiments, cells were suspended in NR-CM, Astro-CM, or Peri-CM. In some experiments, ligands and small molecules were added to hECSR medium or Peri-CM: CHIR 99021 (Tocris) was used at 4 µM except where indicated; DMSO (Sigma-Aldrich) was used as a vehicle control for CHIR; Wnt3a (R&D Systems) was used at 20 ng/mL; Wnt7a (Peprotech, Rocky Hill, NJ) was used at 50 ng/mL; Wnt7b (Abnova, Tapei, Taiwan) was used at 50 ng/mL; R-spondin 1 (Rspo1; Peprotech) was used at 50 ng/mL; doxycycline was used at 1, 2, or 4 µg/mL. The hECSR medium or CM, including any ligands or small molecules, was replaced every other day until confluent (typically 6 days). We denote this time point "Passage 1."

For extended culture, ECs were selectively dissociated and replated as previously described (Nishihara et al., 2020). Cells were incubated with Accutase until endothelial cells appeared round, typically 2–3 min at 37°C. The plate was tapped to release the ECs while SMLCs remained attached, and the EC-enriched cell suspension transferred to 4× volume of DMEM/F-12 and centrifuged for 5 min, 200×g. Cells were resuspended in hECSR medium and seeded on a new collagen IV-coated plate at approximately 3×10^4 cells/cm^2. hECSR medium was replaced every other day until confluent (typically 6 days). The selective dissociation and seeding described above was repeated, and hECSR medium was again replaced every other day

28

624   until confluent (typically 6 days). We denote this time point "Passage 3." In one experiment,

625   these steps were repeated for another two passages. Except where indicated, CHIR 99021 or

626   vehicle (DMSO) was included in the hECSR medium for the entire duration of culture.

627   **RNA-seq**

628   RNA-seq was performed on ECs and SMLCs from the IMR90-4 hPSC line. Four

629   independent differentiations were performed, with DMSO-, CHIR-, and Wnt7a/b-treated ECs at

630   Passage 1 analyzed from all four differentiations. DMSO- and CHIR-treated ECs at Passage 3

631   were analyzed from three of the four differentiations. DMSO-treated SMLCs at Passage 1 were

632   analyzed from two of the four differentiations. Fluorescence-activated cell sorting (FACS) was

633   used to isolate $CD31^+$ ECs and $CD31^-$ SMLCs from mixed Passage 1 cultures. Cells were

634   incubated with Accutase for 10 min at 37°C, passed through 40 μm cell strainers into 4× volume

635   of DMEM/F-12, and centrifuged for 5 min, 200×g. Cells were resuspended in MACS buffer and

636   incubated with CD31-APC antibody (Miltenyi Biotec) for 30 min at 4°C, protected from light.

637   The cell suspension was brought to a volume of 15 mL with MACS buffer and centrifuged at

638   4°C for 5 min, 200×g. Cells were resuspended in MACS buffer containing 2 μg/mL 4',6-

639   diamidino-2-phenylindole (DAPI; Life Technologies). A BD FACSAria III Cell Sorter (BD

640   Biosciences, San Jose, CA) was used to isolate $DAPI^-CD31^+$ cells (live ECs) and $DAPI^-CD31^-$

641   cells (live SMLCs). The resulting cell suspensions were centrifuged at 4°C for 5 min, 200×g, and

642   cell pellets immediately processed for RNA extraction as described below.

643   RNA was isolated using the RNeasy Plus Micro Kit (Qiagen, Germantown, MD). Buffer

644   RLT Plus supplemented with 1% β-mercaptoethanol was used to lyse cells (pellets from FACS

645   of Passage 1 cells, or directly on plates for Passage 3 ECs). Lysates were passed through gDNA

646   Eliminator spin columns, loaded onto RNeasy MinElute spin columns, washed with provided

647   buffers according to manufacturer instructions, and eluted with RNase-free water. Sample

648   concentrations were determined using a NanoDrop spectrophotometer (Thermo Scientific,

649   Waltham, MA) and RNA quality assayed using an Agilent 2100 Bioanalyzer with Agilent RNA

650   6000 Pico Kit (Agilent, Santa Clara, CA). First-strand cDNA synthesis was performed using the

651   SMART-Seq v4 Ultra Low Input RNA kit (Takara Bio, Mountain View, CA) with 5 ng input

652   RNA followed by 9 cycles of PCR amplification and library preparation using the Nextera XT

653   DNA Library Prep Kit (Illumina, San Diego, CA). Sequencing was performed on a NovaSeq

654   6000 (Illumina), with approximately 40–60 million 150 bp paired-end reads obtained for each

655   sample.

656   FASTQ files were aligned to the human genome (hg38) and transcript abundances

657   quantified using RSEM (v1.3.3) (Li and Dewey, 2011) calling bowtie2 (v2.4.2) (Langmead and

658   Salzberg, 2012). Estimated counts from RSEM were input to DESeq2 (v1.26.0) (Love et al.,

659   2014) implemented in R (v3.6.3) for differential expression analysis. Elsewhere, transcript

660   abundances are presented as transcripts per million (TPM). Differentiation pairing as described

661   above was included in the DESeq2 designs. The Wald test with Benjamini-Hochberg correction

662   was used to generate adjusted P-values. Principal component analysis was performed on counts

663   after the DESeq2 variance stabilizing transformation. Bulk RNA-seq data from the literature

664   (FASTQ files; see *Previously published datasets used*) were obtained from the Gene Expression

665   Omnibus (GEO). These FASTQ files were aligned to the mouse genome (mm10) and transcript

666   abundances quantified as described above. DESeq2 was used for differential expression analysis

667   as described above. For direct comparison of human and mouse data, the biomaRt package

668   (v2.42.1) (Durinck et al., 2009) and Ensembl database (Yates et al., 2019) was used to map

669   human gene names to mouse homologs. Venn diagrams were generated using the tool available

670   at http://bioinformatics.psb.ugent.be/webtools/Venn/. To identify solute carrier and efflux

671   transporter genes highly expressed at the human BBB *in vivo*, we used five human brain scRNA-

672 seq datasets (see *Previously published datasets used*) integrated in a previous meta-analysis

673 (Gastfriend et al., 2021). *SLC* and *ABC* genes with average expression greater than 100 TPM in

674 endothelial cells across the five independent datasets were selected.

675 **Immunocytochemistry**

676   Immunocytochemistry was performed in 24-well plates. Cells were washed once with

677 500 µL DPBS and fixed with 500 µL cold (–20°C) methanol for 5 min, except cells intended for

678 calponin/SM22a detection, which were fixed with 500 µL of 4% paraformaldehyde for 15 min.

679 Cells were washed three times with 500 µL DPBS and blocked in 150 µL DPBS supplemented

680 with 10% goat serum (Life Technologies) for 1 h at room temperature, except cells intended for

681 calponin/SM22α detection, which were blocked and permeabilized in DPBS supplemented with

682 3% BSA and 0.1% Triton X-100 . Primary antibodies diluted in 150 µL of the above blocking

683 solutions (see *Key Resources Table* for antibody information) were added to cells and incubated

684 overnight at 4°C on a rocking platform. Cells were washed three times with 500 µL DPBS.

685 Secondary antibodies diluted in 150 µL of the above blocking solutions (see *Key Resources*

686 *Table* for antibody information) were added to cells and incubated for 1 h at room temperature

687 on a rocking platform, protected from light. Cells were washed three times with 500 µL DPBS,

688 followed by 5 min incubation with 500 µL DPBS plus 4 µM Hoechst 33342 (Life Technologies).

689 Images were acquired using an Eclipse Ti2-E epifluorescence microscope (Nikon, Tokyo, Japan)

690 with a 20× objective or an A1R-Si+ confocal microscope (Nikon) with a 100× oil objective.

691 Confocal images were acquired with 1 µm slice spacing.

692   Images were analyzed using FIJI (ImageJ) software. For epifluorescence images, 5 fields

693 (20×) were analyzed per well, with 3–4 wells per treatment condition. For quantification of cell

694 number, EC colonies were manually outlined, and the Analyze Particles function was used to

695 estimate the number of nuclei within the EC colonies. Nuclei outside the EC colonies were

696   manually counted. EC purity (% EC) was calculated as the number of nuclei within EC colonies

697   relative to total nuclei. To estimate % GLUT-1^{+} ECs, cells within the EC colonies with

698   membrane-localized GLUT-1 immunoreactivity (e.g., arrowheads in Figure 2B) were manually

699   counted. For quantification of fluorescence intensity in epifluorescence images, EC colonies

700   were manually outlined, and the Measure function was used to obtain the mean fluorescence

701   intensity for each image channel (fluorophore). A cell-free area of the plate was similarly

702   quantified for background subtraction. Following background subtraction, the mean fluorescence

703   intensity of each protein of interest was normalized to the mean fluorescence intensity of

704   Hoechst to correct for effects of cell density. For confocal images, 3–4 fields (100×) containing

705   only VE-cadherin[+] ECs were analyzed per well, with 4 wells per treatment condition. The first

706   slice with visible nuclei (closest to glass) was defined as $Z = 0$, and the Measure function was

707   used to obtain the mean fluorescence intensity for each image channel (fluorophore) in each slice

708   from $Z = 0$ to $Z = 7$ μm. A cell-free area of the plate was similarly quantified for background

709   subtraction. After background subtraction, to approximate total abundance (area under the

710   fluorescence versus Z curve, AUC) for each channel, mean fluorescence intensities were

711   summed across all slices. AUC for the proteins of interest were normalized to Hoechst AUC.

712   **Western blotting**

713   To enrich samples from Passage 1 cultures for ECs, the Accutase-based selective

714   dissociation method described above was employed. Dissociated cells were centrifuged for 5

715   min, 200×g, and resulting cell pellets were lysed in RIPA buffer (Rockland Immunochemicals,

716   Pottstown, PA) supplemented with 1× Halt Protease Inhibitor Cocktail (Thermo Scientific).

717   Passage 3 cells were lysed with the above buffer directly on plates. Lysates were centrifuged at

718   4°C for 5 min, 14,000×g, and protein concentration in supernatants quantified using the Pierce

719   BCA Protein Assay Kit (Thermo Scientific). Equal amounts of protein were diluted to equal

720   volume with water, mixed with sample buffer, and heated at 95°C for 5 min, except lysates

721   intended for GLUT-1 Western blotting, which were not heated. Samples were resolved on 4–

722   12% Tris-Glycine gels and transferred to nitrocellulose membranes. Membranes were blocked

723   for 1 h in tris-buffered saline plus 0.1% Tween-20 (TBST) supplemented with 5% non-fat dry

724   milk. Primary antibodies (see *Key Resources Table* for antibody information) diluted in TBST

725   plus 5% non-fat dry milk were added to membranes and incubated overnight at 4°C on a rocking

726   platform. Membranes were washed five times with TBST. Secondary antibodies (see *Key*

727   *Resources Table* for antibody information) diluted in TBST were added to membranes and

728   incubated for 1 h at room temperature on a rocking platform, protected from light. Membranes

729   were washed five times with TBST and imaged using an Odyssey 9120 (LI-COR, Lincoln, NE).

730   Band intensities were quantified using Image Studio software (LI-COR).

731   **Dextran accumulation assay**

732   A fixable, Alexa Fluor 488-conjugated dextran with an average molecular weight of 10

733   kDa (Invitrogen) was used as a tracer to estimate total fluid-phase endocytosis. Dextran was

734   added at 10 µM to the medium of Passage 1 cultures. Plates were incubated on rotating platforms

735   at 37°C or 4°C for 2 h. Medium was removed and cells were washed once with DPBS, and then

736   incubated with Accutase for 10 min at 37°C. Cell suspensions were passed through 40 µm cell

737   strainers into 4× volume of DMEM/F-12 and centrifuged for 5 min, 200×g. Cells were

738   resuspended in MACS buffer and incubated with the CD31-APC antibody (Miltenyi Biotec) for

739   30 min at 4°C, protected from light. Cell suspensions were brought to a volume of 5 mL with

740   MACS buffer and centrifuged at 4°C for 5 min, 200×g. Pellets were resuspended in DPBS

741   supplemented with 4% paraformaldehyde and incubated for 15 min at room temperature,

742   protected from light. Cells were centrifuged for 5 min, 200×g. Pellets were resuspended in

743   MACS buffer and analyzed on a BD FACSCalibur flow cytometer (BD Biosciences). FlowJo

744   software (BD Biosciences) was used to gate CD31$^+$ cells and quantify geometric mean

745   fluorescence intensity and coefficient of variation (CV) of dextran.

746   **Statistics**

747   Individual wells of cultured cells that underwent identical experimental treatments are

748   defined as replicates, and all key experiments were repeated using multiple independent hPSC

749   differentiations. Detailed information about replication strategy is provided in figure legends.

750   Student's t test was used for comparison of means from two experimental groups. One-way

751   analysis of variance (ANOVA) was used for comparison of means from three or more

752   experimental groups, followed by Dunnett's post-hoc test for comparison of multiple treatments

753   to a single control, or Tukey's honest significant difference (HSD) post-hoc test for multiple

754   pairwise comparisons. When data from multiple differentiations were combined, two-way

755   ANOVA (one factor being the experimental treatment and one factor being the differentiation)

756   was used for comparison of means to achieve blocking of differentiation-based variability,

757   followed by post-hoc tests as described above if more than two experimental treatments were

758   compared. For fluorescence intensities (a.u.), two-way ANOVA was performed prior to

759   normalization of these values to the control group within each differentiation (for visualization in

760   plots). Statistical tests were performed in JMP Pro (v15.0.0). For RNA-seq differential

761   expression analysis, the DESeq2 Wald test with Benjamini-Hochberg correction was used to

762   calculate P-values. Descriptions of the statistical tests used are provided in figure legends.

Acknowledgements

Competing interests

BDG, HN, BE, SPP, and EVS have filed an invention disclosure related to this work with the Wisconsin Alumni Research Foundation.

Supplementary files

- **Supplementary file 1. RNA-sequencing gene expression data for hPSC-derived ECs and SMLCs.** Abundances are provided in transcripts per million (TPM).

- **Supplementary file 2. RNA-sequencing differential expression analysis of hPSC-derived ECs.** DESeq2-derived average expression (baseMean), $\log_2$(fold change), Wald statistic, P-value (Wald test), and adjusted P-value (Benjamini-Hochberg correction) are

786 shown. **(A)** Passage 1 CHIR-treated ECs versus Passage 1 DMSO-treated ECs. **(B)**

787 Passage 1 Wnt7a/b-treated ECs versus Passage 1 DMSO-treated ECs. **(C)** Passage 3

788 CHIR-treated ECs versus Passage 3 DMSO-treated ECs. **(D)** Passage 3 DMSO-treated

789 ECs versus Passage 1 DMSO-treated ECs. **(E)** Lists of upregulated and downregulated

790 genes comprising the intersection of the comparisons in (A) and (B), and (A) and (C),

791 used to generate Venn diagrams in Figure 8E.

792 - **Supplementary file 3. Wnt-regulated EC genes in multiple contexts. (A)** Differential

793 expression analysis of P7 murine brain, liver, lung, and kidney ECs (Sabbagh et al.,

794 2018). DESeq2-derived average expression (baseMean), $\log_2$(fold change), Wald

795 statistic, P-value (Wald test), and adjusted P-value (Benjamini-Hochberg correction) are

796 shown. **(B)** Lists of brain-enriched and brain-depleted genes comprising the intersection

797 of the comparisons in (A). **(C-E)** Differential expression analysis of adult murine ECs

798 with β-catenin-stabilization versus controls from pituitary (Wang et al., 2019) (C), liver

799 (Munji et al., 2019) (D), and brain ECs cultured *in vitro* (Sabbagh and Nathans, 2020)

800 (E). DESeq2-derived average expression (baseMean), $\log_2$(fold change), Wald statistic,

801 P-value (Wald test), and adjusted P-value (Benjamini-Hochberg correction) are shown.

802 **(F)** Lists of concordantly Wnt-regulated genes in Passage 1 hPSC-derived ECs and the

803 three comparisons shown in (C-E), from the set of brain-enriched and brain-depleted

804 genes identified in (B).

805

806 **Data availability**

807 RNA-seq data have been deposited in GEO.

808

809

36

810 **Previously published datasets used**

Citation	Description	Identifiers	Source
(Sabbagh et al., 2018)	Adult mouse postnatal day 7 brain, liver, lung, and kidney ECs	GSM3040844 GSM3040845 GSM3040852 GSM3040853 GSM3040858 GSM3040859 GSM3040864 GSM3040865	https://www.ncbi.nlm.nih.gov/geo/query/acc.cgi?acc=GSE111839
(Munji et al., 2019)	Adult mouse liver ECs (controls and β-catenin gain-of-function)	GSM2498580 GSM2498581 GSM2498582 GSM2498583 GSM2498584 GSM2498585 GSM2498586 GSM2498587	https://www.ncbi.nlm.nih.gov/geo/query/acc.cgi?acc=GSE95201
(Wang et al., 2019)	Adult mouse anterior and posterior pituitary ECs (controls and β-catenin gain-of-function)	GSM3455653 GSM3455654 GSM3455657 GSM3455658 GSM3455661 GSM3455662 GSM3455665 GSM3455666	https://www.ncbi.nlm.nih.gov/geo/query/acc.cgi?acc=GSE122117
(Sabbagh and Nathans, 2020)	Adult mouse brain ECs cultured *in vitro* (controls and β-catenin gain-of-function)	GSM4160534 GSM4160535 GSM4160536 GSM4160537 GSM4160538 GSM4160539 GSM4160540 GSM4160541 GSM4160542 GSM4160543	https://www.ncbi.nlm.nih.gov/geo/query/acc.cgi?acc=GSE118731
(Gastfriend et al., 2021)	Meta-analysis of human brain single cells across multiple developmental stages and brain regions (enumerated below)		
Allen Institute, 2019	Adult neocortex		https://portal.brain-map.org/atlases-and-data/rnaseq/human-multiple-cortical-areas-smart-seq
(Polioudakis et al., 2019)	GW17-18 neocortex		http://solo.bmap.ucla.edu/shiny/webapp/
(Han et al., 2020)	Adult temporal lobe and cerebellum	GSM3980129 GSM4008656 GSM4008657 GSM4008658	https://www.ncbi.nlm.nih.gov/geo/query/acc.cgi?acc=GSE134355
(La Manno et al., 2016)	GW6-11 ventral midbrain		https://www.ncbi.nlm.nih.gov/geo/query/acc.cgi?acc=GSE76381
(Zhong et al., 2020)	GW16-27 hippocampus		https://www.ncbi.nlm.nih.gov/geo/query/acc.cgi?acc=GSE119212

811

REFERENCES

Andreone BJ, Chow BW, Tata A, Lacoste B, Ben-Zvi A, Bullock K, Deik AA, Ginty DD, Clish CB, Gu C. 2017. Blood-Brain Barrier Permeability Is Regulated by Lipid Transport-Dependent Suppression of Caveolae-Mediated Transcytosis. *Neuron* **94**:581-594.e5. doi:10.1016/j.neuron.2017.03.043

Armulik A, Genové G, Mäe M, Nisancioglu MH, Wallgard E, Niaudet C, He L, Norlin J, Lindblom P, Strittmatter K, Johansson BR, Betsholtz C. 2010. Pericytes regulate the blood–brain barrier. *Nature* **468**:557–561. doi:10.1038/nature09522

Bao X, Bhute VJ, Han T, Qian T, Lian X, Palecek SP. 2017. Human pluripotent stem cell-derived epicardial progenitors can differentiate to endocardial-like endothelial cells 191–201. doi:10.1002/btm2.10062

Bao X, Lian X, Palecek SP. 2016. Directed Endothelial Progenitor Differentiation from Human Pluripotent Stem Cells Via Wnt Activation Under Defined Conditions. *Methods Mol Biol* **1481**:183–96. doi:10.1007/978-1-4939-6393-5_17

Bauer B, Hartz AMS, Fricker G, Miller DS. 2004. Pregnane X receptor up-regulation of P-glycoprotein expression and transport function at the blood-brain barrier. *Mol Pharmacol* **66**:413–419. doi:10.1124/mol.66.3.

Ben-Zvi A, Lacoste B, Kur E, Andreone BJ, Mayshar Y, Yan H, Gu C. 2014. Mfsd2a is critical for the formation and function of the blood–brain barrier. *Nature* **509**:507–11. doi:10.1038/nature13324

Benz F, Wichitnaowarat V, Lehmann M, Germano RF, Mihova D, Macas J, Adams RH, Mark Taketo M, Plate KH, Guérit S, Vanhollebeke B, Liebner S. 2019. Low wnt/β-catenin signaling determines leaky vessels in the subfornical organ and affects water homeostasis in mice. *Elife* **8**:1–29. doi:10.7554/eLife.43818

Berezowski V, Landry C, Dehouck MP, Cecchelli R, Fenart L. 2004. Contribution of glial cells and pericytes to the mRNA profiles of P-glycoprotein and multidrug resistance-associated proteins in an in vitro model of the blood-brain barrier. *Brain Res* **1018**:1–9. doi:10.1016/j.brainres.2004.05.092

Boyer-Di Ponio J, El-Ayoubi F, Glacial F, Ganeshamoorthy K, Guillevic O, Couraud PO, Driancourt C, Godet M, Perrie N, Uzan G, Boyer-Di Ponio J, El-Ayoubi F, Glacial F, Ganeshamoorthy K, Driancourt C, Godet M, Perrière N, Guillevic O, Olivier Couraud P, Uzan G, Ponio JB, El-Ayoubi F, Glacial F, Ganeshamoorthy K, Guillevic O, Couraud PO, Driancourt C, Godet M, Perrie N, Uzan G. 2014. Instruction of circulating endothelial progenitors in vitro towards specialized blood-brain barrier and arterial phenotypes. *PLoS One* **9**. doi:10.1371/journal.pone.0084179

Canfield SG, Stebbins MJ, Morales BS, Asai SW, Vatine GD, Svendsen CN, Palecek SP, Shusta E V. 2017. An isogenic blood–brain barrier model comprising brain endothelial cells, astrocytes, and neurons derived from human induced pluripotent stem cells. *J Neurochem* **140**:874–888. doi:10.1111/jnc.13923

38

851 Castro Dias M, Coisne C, Lazarevic I, Baden P, Hata M, Iwamoto N, Miguel D, Francisco F,
852   Vanlandewijck M, He L, Baier FA, Stroka D, Bruggmann R, Lyck R, En G, Deutsch U,
853   Betsholtz C, Furuse M, Shoichiro T, Engelhardt B, Castro Dias M, Coisne C, Lazarevic I,
854   Baden P, Hata M, Iwamoto N, Francisco DMF, Vanlandewijck M, He L, Baier FA, Stroka
855   D, Bruggmann R, Lyck R, Enzmann G, Deutsch U, Betsholtz C, Furuse M, Tsukita S,
856   Engelhardt B. 2019. Claudin-3-deficient C57BL/6J mice display intact brain barriers. *Sci
857   Rep* **9**:1–16. doi:10.1038/s41598-018-36731-3

858 Cecchelli R, Aday S, Sevin E, Almeida C, Culot M, Dehouck L, Coisne C, Engelhardt B,
859   Dehouck MP, Ferreira L. 2014. A stable and reproducible human blood-brain barrier model
860   derived from hematopoietic stem cells. *PLoS One* **9**. doi:10.1371/journal.pone.0099733

861 Chen G, Gulbranson DR, Hou Z, Bolin JM, Ruotti V, Probasco MD, Smuga-Otto K, Howden
862   SE, Diol NR, Propson NE, Wagner R, Lee GO, Antosiewicz-Bourget J, Teng JMC,
863   Thomson JA. 2011. Chemically defined conditions for human iPSC derivation and culture.
864   *Nat Methods* **8**:424–429. doi:10.1038/nmeth.1593

865 Cho C, Smallwood PM, Nathans J. 2017. Reck and Gpr124 Are Essential Receptor Cofactors for
866   Wnt7a/Wnt7b-Specific Signaling in Mammalian CNS Angiogenesis and Blood-Brain
867   Barrier Regulation. *Neuron* **95**:1056-1073.e5. doi:10.1016/j.neuron.2017.07.031

868 Clevers H, Loh KM, Nusse R. 2014. Stem cell signaling. An integral program for tissue renewal
869   and regeneration: Wnt signaling and stem cell control. *Science* **346**:1248012.
870   doi:10.1126/science.1248012

871 Corada M, Orsenigo F, Bhat GP, Conze LL, Breviario F, Cunha SI, Claesson-welsh L,
872   Beznoussenko G V, Mironov AA, Bacigaluppi M, Martino G, Pitulescu ME, Adams RH,
873   Magnusson P, Dejana E. 2018. Fine-Tuning of Sox17 and Canonical Wnt Coordinates the
874   Permeability Properties of the Blood-Brain Barrier 511–525.
875   doi:10.1161/CIRCRESAHA.118.313316

876 Cullen M, Elzarrad MK, Seaman S, Zudaire E, Stevens J, Yang MY, Li X, Chaudhary A, Xu L,
877   Hilton MB, Logsdon D, Hsiao E, Stein E V., Cuttitta F, Haines DC, Nagashima K,
878   Tessarollo L, St. Croix B. 2011. GPR124, an orphan G protein-coupled receptor, is required
879   for CNS-specific vascularization and establishment of the blood-brain barrier. *Proc Natl
880   Acad Sci* **108**:5759–5764. doi:10.1073/pnas.1017192108

881 Daneman R, Agalliu D, Zhou L, Kuhnert F, Kuo CJ, Barres BA. 2009. Wnt/beta-catenin
882   signaling is required for CNS, but not non-CNS, angiogenesis. *Proc Natl Acad Sci U S A*
883   **106**:641–6. doi:10.1073/pnas.0805165106

884 Daneman R, Engelhardt B. 2017. Brain barriers in health and disease. *Neurobiol Dis* **107**:1–3.
885   doi:10.1016/j.nbd.2017.05.008

886 Daneman R, Zhou L, Agalliu D, Cahoy JD, Kaushal A, Barres BA. 2010a. The Mouse Blood-
887   Brain Barrier Transcriptome: A New Resource for Understanding the Development and
888   Function of Brain Endothelial Cells. *PLoS One* **5**:e13741.
889   doi:10.1371/journal.pone.0013741

890   Daneman R, Zhou L, Kebede AA, Barres BA. 2010b. Pericytes are required for blood–brain
891   barrier integrity during embryogenesis. *Nature* **468**:562–566. doi:10.1038/nature09513

892   Delsing L, Dönnes P, Sánchez J, Clausen M, Voulgaris D, Falk A, Herland A, Brolén G,
893   Zetterberg H, Hicks R, Synnergren J. 2018. Barrier Properties and Transcriptome
894   Expression in Human iPSC-Derived Models of the Blood–Brain Barrier. *Stem Cells*
895   **36**:1816–1827. doi:10.1002/stem.2908

896   Durinck S, Spellman PT, Birney E, Huber W. 2009. Mapping identifiers for the integration of
897   genomic datasets with the R/ Bioconductor package biomaRt. *Nat Protoc* **4**:1184–1191.
898   doi:10.1038/nprot.2009.97

899   Ebert AD, Shelley BC, Hurley AM, Onorati M, Castiglioni V, Patitucci TN, Svendsen SP, Mattis
900   VB, McGivern J V., Schwab AJ, Sareen D, Kim HW, Cattaneo E, Svendsen CN. 2013. EZ
901   spheres: A stable and expandable culture system for the generation of pre-rosette
902   multipotent stem cells from human ESCs and iPSCs. *Stem Cell Res* **10**:417–427.
903   doi:10.1016/j.scr.2013.01.009

904   Engelhardt B, Liebner S. 2014. Novel insights into the development and maintenance of the
905   blood-brain barrier. *Cell Tissue Res*. doi:10.1007/s00441-014-1811-2

906   Eubelen M, Bostaille N, Cabochette P, Gauquier A, Tebabi P, Dumitru AC, Koehler M, Gut P,
907   Alsteens D, Stainier DYR, Garcia-Pino A, Vanhollebeke B. 2018. A molecular mechanism
908   for Wnt ligand-specific signaling. *Science (80-)* **361**. doi:10.1126/science.aat1178

909   Gastfriend BD, Foreman KL, Katt ME, Palecek SP, Shusta E V. 2021. Integrative analysis of the
910   human brain mural cell transcriptome. *J Cereb Blood Flow Metab* **In press.**

911   Guérit S, Fidan E, Macas J, Czupalla CJ, Figueiredo R, Vijikumar A, Yalcin BH, Thom S,
912   Winter P, Gerhardt H, Devraj K, Liebner S. 2021. Astrocyte-derived Wnt growth factors are
913   required for endothelial blood-brain barrier maintenance. *Prog Neurobiol* **199**.
914   doi:10.1016/j.pneurobio.2020.101937

915   Han X, Zhou Z, Fei L, Sun H, Wang R, Chen Y, Chen H, Wang J, Tang H, Ge W, Zhou Y, Ye F,
916   Jiang M, Wu J, Xiao Y, Jia X, Zhang T, Ma X, Zhang Q, Bai X, Lai S, Yu C, Zhu L, Lin R,
917   Gao Y, Wang M, Wu Y, Zhang J, Zhan R, Zhu S, Hu H, Wang C, Chen M, Huang H, Liang
918   T, Chen J, Wang W, Zhang D, Guo G. 2020. Construction of a human cell landscape at
919   single-cell level, Nature. Springer US. doi:10.1038/s41586-020-2157-4

920   Harada N, Tamai Y, Ishikawa TO, Sauer B, Takaku K, Oshima M, Taketo MM. 1999. Intestinal
921   polyposis in mice with a dominant stable mutation of the β-catenin gene. *EMBO J* **18**:5931–
922   5942. doi:10.1093/emboj/18.21.5931

923   He L, Vanlandewijck M, Mäe MA, Andrae J, Ando K, Del Gaudio F, Nahar K, Lebouvier T,
924   Laviña B, Gouveia L, Sun Y, Raschperger E, Segerstolpe Å, Liu J, Gustafsson S, Räsänen
925   M, Zarb Y, Mochizuki N, Keller A, Lendahl U, Betsholtz C. 2018. Single-cell RNA
926   sequencing of mouse brain and lung vascular and vessel-associated cell types. *Sci data*
927   **5**:180160. doi:10.1038/sdata.2018.160

928 Herrnberger L, Seitz R, Kuespert S, Bösl MR, Fuchshofer R, Tamm ER. 2012. Lack of
929   endothelial diaphragms in fenestrae and caveolae of mutant Plvap-deficient mice.
930   *Histochem Cell Biol* **138**:709–724. doi:10.1007/s00418-012-0987-3

931 Jaffe RB, Yu J, Vodyanik MA, Smuga-Otto K, Antosiewicz-Bourget J, Frane JL, Tian S, Nie J,
932   Jonsdottir GA, Ruotti V, Stewart R, Slukvin II, Thomson JA. 2008. Induced Pluripotent
933   Stem Cell Lines Derived From Human Somatic Cells. *Obstet Gynecol Surv* **63**:154–155.
934   doi:10.1097/01.ogx.0000305193.72586.39

935 Kim K-A, Kakitani M, Zhao J, Oshima T, Tang T, Binnerts M, Liu Y, Boyle B, Park E, Emtage
936   P, Funk WD, Tomizuka K. 2005. Mitogenic influence of human R-spondin1 on the
937   intestinal epithelium. *Science* **309**:1256–9. doi:10.1126/science.1112521

938 Kim K-A, Wagle M, Tran K, Zhan X, Dixon MA, Liu S, Gros D, Korver W, Yonkovich S,
939   Tomasevic N, Binnerts M, Abo A. 2008. R-Spondin Family Members Regulate the Wnt
940   Pathway by a Common Mechanism. *Mol Biol Cell* **19**:2588–2596. doi:10.1091/mbc.e08-02-
941   0187

942 Koo BK, Spit M, Jordens I, Low TY, Stange DE, Van De Wetering M, Van Es JH, Mohammed
943   S, Heck AJR, Maurice MM, Clevers H. 2012. Tumour suppressor RNF43 is a stem-cell E3
944   ligase that induces endocytosis of Wnt receptors. *Nature* **488**:665–669.
945   doi:10.1038/nature11308

946 Kreitzer FR, Salomonis N, Sheehan A, Huang M, Park JS, Spindler MJ, Lizarraga P, Weiss WA,
947   So P, Conklin BR. 2013. A robust method to derive functional neural crest cells from
948   human pluripotent stem cells. *Am J Stem Cells* **2**:119–31.

949 Kuhnert F, Mancuso MR, Shamloo A, Wang H-THT, Choksi V, Florek M, Su H, Fruttiger M,
950   Young WL, Heilshorn SC, Kuo CJ. 2010. Essential regulation of CNS angiogenesis by the
951   orphan G protein-coupled receptor GPR124. *Science (80-)* **330**:985–989.
952   doi:10.1126/science.1196554

953 La Manno G, Gyllborg D, Codeluppi S, Nishimura K, Salto C, Zeisel A, Borm LE, Stott SRW,
954   Toledo EM, Villaescusa JC, Lönnerberg P, Ryge J, Barker RA, Arenas E, Linnarsson S.
955   2016. Molecular Diversity of Midbrain Development in Mouse, Human, and Stem Cells.
956   *Cell* **167**:566-580.e19. doi:10.1016/j.cell.2016.09.027

957 Laksitorini MD, Yathindranath V, Xiong W, Hombach-Klonisch S, Miller DW. 2019.
958   Modulation of Wnt/β-catenin signaling promotes blood-brain barrier phenotype in cultured
959   brain endothelial cells. *Sci Rep* **9**:1–13. doi:10.1038/s41598-019-56075-w

960 Langmead B, Salzberg SL. 2012. Fast gapped-read alignment with Bowtie 2. *Nat Methods*
961   **9**:357–359. doi:10.1038/nmeth.1923

962 Li B, Dewey CN. 2011. RSEM: accurate transcript quantification from RNA-Seq data with or
963   without a reference genome. *BMC Bioinformatics* **12**:323.

964 Lian X, Bao X, Al-Ahmad A, Liu J, Wu Y, Dong W, Dunn KK, Shusta E V., Palecek SP. 2014.
965   Efficient differentiation of human pluripotent stem cells to endothelial progenitors via

small-molecule activation of WNT signaling. *Stem Cell Reports* **3**:804–816. doi:10.1016/j.stemcr.2014.09.005

Lian X, Zhang J, Zhu K, Kamp TJ, Palecek SP. 2013. Insulin inhibits cardiac mesoderm, not mesendoderm, formation during cardiac differentiation of human pluripotent stem cells and modulation of canonical wnt signaling can rescue this inhibition. *Stem Cells* **31**:447–457. doi:10.1002/stem.1289

Liebner S, Corada M, Bangsow T, Babbage J, Taddei A, Czupalla CJ, Reis M, Felici A, Wolburg H, Fruttiger M, Taketo MM, Von Melchner H, Plate KH, Gerhardt H, Dejana E. 2008. Wnt/β-catenin signaling controls development of the blood - brain barrier. *J Cell Biol* **183**:409–417. doi:10.1083/jcb.200806024

Lim RG, Quan C, Reyes-Ortiz AM, Lutz SE, Kedaigle AJ, Gipson TA, Wu J, Vatine GD, Stocksdale J, Casale MS, Svendsen CN, Fraenkel E, Housman DE, Agalliu D, Thompson LM. 2017. Huntington's Disease iPSC-Derived Brain Microvascular Endothelial Cells Reveal WNT-Mediated Angiogenic and Blood-Brain Barrier Deficits. *Cell Rep* **19**:1365–1377. doi:10.1016/j.celrep.2017.04.021

Lippmann ES, Azarin SM, Kay JE, Nessler RA, Wilson HK, Al-Ahmad A, Palecek SP, Shusta E V. 2012. Derivation of blood-brain barrier endothelial cells from human pluripotent stem cells. *Nat Biotechnol* **30**:783–791. doi:10.1038/nbt.2247

Lippmann ES, Azarin SM, Palecek SP, Shusta E V. 2020. Commentary on human pluripotent stem cell-based blood–brain barrier models. *Fluids Barriers CNS* **17**:4–9. doi:10.1186/s12987-020-00222-3

Lippmann ES, Estevez-Silva MC, Ashton RS. 2014. Defined human pluripotent stem cell culture enables highly efficient neuroepithelium derivation without small molecule inhibitors. *Stem Cells* **32**:1032–1042. doi:10.1002/stem.1622

Love MI, Huber W, Anders S. 2014. Moderated estimation of fold change and dispersion for RNA-seq data with DESeq2. *Genome Biol* **15**:550. doi:10.1186/s13059-014-0550-8

Lu TM, Houghton S, Magdeldin T, Barcia Durán JG, Minotti AP, Snead A, Sproul A, Nguyen DHT, Xiang J, Fine HA, Rosenwaks Z, Studer L, Rafii S, Agalliu D, Redmond D, Lis R. 2021. Pluripotent stem cell-derived epithelium misidentified as brain microvascular endothelium requires ETS factors to acquire vascular fate. *Proc Natl Acad Sci U S A* **118**. doi:10.1073/pnas.2016950118

Mazzoni J, Smith JR, Shahriar S, Cutforth T, Ceja B, Agalliu D. 2017. The Wnt Inhibitor Apcdd1 Coordinates Vascular Remodeling and Barrier Maturation of Retinal Blood Vessels. *Neuron* **96**:1055-1069.e6. doi:10.1016/j.neuron.2017.10.025

Mouillesseaux KP, Wiley DS, Saunders LM, Wylie LA, Kushner EJ, Chong DC, Citrin KM, Barber AT, Park Y, Kim JDJJD, Samsa LA, Kim JDJJD, Liu J, Jin SW, Bautch VL. 2016. Notch regulates BMP responsiveness and lateral branching in vessel networks via SMAD6. *Nat Commun* **7**:1–12. doi:10.1038/ncomms13247

42

Munji RN, Soung AL, Weiner GA, Sohet F, Semple BD, Trivedi A, Gimlin K, Kotoda M, Korai M, Aydin S, Batugal A, Cabangcala AC, Schupp PG, Oldham MC, Hashimoto T, Noble-Haeusslein LJ, Daneman R. 2019. Profiling the mouse brain endothelial transcriptome in health and disease models reveals a core blood–brain barrier dysfunction module. *Nat Neurosci* **22**:1892–1902. doi:10.1038/s41593-019-0497-x

Nishihara H, Gastfriend BD, Soldati S, Perriot S, Mathias A, Sano Y, Shimizu F, Gosselet F, Kanda T, Palecek SP, Du Pasquier R, Shusta E V., Engelhardt B. 2020. Advancing human induced pluripotent stem cell-derived blood-brain barrier models for studying immune cell interactions. *FASEB J* **34**:16693–16715. doi:10.1096/fj.202001507RR

Obermeier B, Daneman R, Ransohoff RM. 2013. Development, maintenance and disruption of the blood-brain barrier. *Nat Med*. doi:10.1038/nm.3407

Paolinelli R, Corada M, Ferrarini L, Devraj K, Artus C, Czupalla CJ, Rudini N, Maddaluno L, Papa E, Engelhardt B, Couraud PO, Liebner S, Dejana E. 2013. Wnt Activation of Immortalized Brain Endothelial Cells as a Tool for Generating a Standardized Model of the Blood Brain Barrier In Vitro. *PLoS One* **8**. doi:10.1371/journal.pone.0070233

Phoenix TN, Patmore DM, Boop S, Boulos N, Jacus MO, Patel YT, Roussel MF, Finkelstein D, Goumnerova L, Perreault S, Wadhwa E, Cho YJ, Stewart CF, Gilbertson RJ. 2016. Medulloblastoma Genotype Dictates Blood Brain Barrier Phenotype. *Cancer Cell* **29**:508–522. doi:10.1016/j.ccell.2016.03.002

Polioudakis D, de la Torre-Ubieta L, Langerman J, Elkins AG, Shi X, Stein JL, Vuong CK, Nichterwitz S, Gevorgian M, Opland CK, Lu D, Connell W, Ruzzo EK, Lowe JK, Hadzic T, Hinz FI, Sabri S, Lowry WE, Gerstein MB, Plath K, Geschwind DH. 2019. A Single-Cell Transcriptomic Atlas of Human Neocortical Development during Mid-gestation. *Neuron* **103**:785-801.e8. doi:10.1016/j.neuron.2019.06.011

Praça C, Rosa SC, Sevin E, Cecchelli R, Dehouck M-PP, Ferreira LS. 2019. Derivation of Brain Capillary-like Endothelial Cells from Human Pluripotent Stem Cell-Derived Endothelial Progenitor Cells. *Stem Cell Reports* **13**:599–611. doi:10.1016/j.stemcr.2019.08.002

Profaci CP, Munji RN, Pulido RS, Daneman R. 2020. The blood-brain barrier in health and disease: Important unanswered questions. *J Exp Med* **217**:1–16. doi:10.1084/jem.20190062

Qian T, Maguire SE, Canfield SG, Bao X, Olson WR, Shusta E V, Palecek SP. 2017. Directed differentiation of human pluripotent stem cells to blood-brain barrier endothelial cells. *Sci Adv* **3**:e1701679. doi:10.1126/sciadv.1701679

Reese TS, Karnovsky MJ. 1967. Fine structural localization of a blood-brain barrier to exogenous peroxidase. *J Cell Biol* **34**:207–217. doi:10.1083/jcb.34.1.207

Roudnicky F, Kim BK, Lan Y, Schmucki R, Küppers V, Christensen K, Graf M, Patsch C, Burcin M, Meyer CA, Westenskow PD, Cowan CA. 2020a. Identification of a combination of transcription factors that synergistically increases endothelial cell barrier resistance. *Sci Rep* **10**:1–9. doi:10.1038/s41598-020-60688-x

Roudnicky F, Zhang JD, Kim BK, Pandya NJ, Lan Y, Sach-Peltason L, Ragelle H, Strassburger P, Gruener S, Lazendic M, Uhles S, Revelant F, Eidam O, Sturm G, Kueppers V, Christensen K, Goldstein LD, Tzouros M, Banfai B, Modrusan Z, Graf M, Patsch C, Burcin M, Meyer CA, Westenskow PD, Cowan CA. 2020b. Inducers of the endothelial cell barrier identified through chemogenomic screening in genome-edited hPSC-endothelial cells. *Proc Natl Acad Sci U S A* **117**:19854–19865. doi:10.1073/PNAS.1911532117

Sabbagh MF, Heng JS, Luo C, Castanon RG, Nery JR, Rattner A, Goff LA, Ecker JR, Nathans J. 2018. Transcriptional and epigenomic landscapes of CNS and non-CNS vascular endothelial cells. *Elife* **7**:1–44. doi:10.7554/eLife.36187

Sabbagh MF, Nathans J. 2020. A genome-wide view of the de-differentiation of central nervous system endothelial cells in culture. *Elife* **9**:1–19. doi:10.7554/eLife.51276

Sareen D, Gowing G, Sahabian A, Staggenborg K, Paradis R, Avalos P, Latter J, Ornelas L, Garcia L, Svendsen CN. 2014. Human induced pluripotent stem cells are a novel source of neural progenitor cells (iNPCs) that migrate and integrate in the rodent spinal cord. *J Comp Neurol* **522**:2707–2728. doi:10.1002/cne.23578

Schindelin J, Arganda-carreras I, Frise E, Kaynig V, Longair M, Pietzsch T, Preibisch S, Rueden C, Saalfeld S, Schmid B, Tinevez J, White DJ, Hartenstein V, Eliceiri K, Tomancak P, Cardona A. 2019. Fiji : an open-source platform for biological-image analysis **9**. doi:10.1038/nmeth.2019

Shang Z, Chen D, Wang Q, Wang SSSSS, Deng Q, Wu L, Liu C, Ding X, Wang SSSSS, Zhong J, Zhang D, Cai X, Zhu S, Yang H, Liu L, Fink JL, Chen F, Liu X, Gao Z, Xu X. 2018. Single-cell RNA-seq reveals dynamic transcriptome profiling in human early neural differentiation. *Gigascience* **7**:1–19. doi:10.1093/gigascience/giy117

Sohet F, Lin C, Munji RN, Lee SY, Ruderisch N, Soung A, Arnold TD, Derugin N, Vexler ZS, Yen FT, Daneman R. 2015. LSR/angulin-1 is a tricellular tight junction protein involved in blood–brain barrier formation. *J Cell Biol* **208**:703–711. doi:10.1083/jcb.201410131

Song HW, Foreman KL, Gastfriend BD, Kuo JS, Palecek SP, Shusta E V. 2020. Transcriptomic comparison of human and mouse brain microvessels. *Sci Rep* **10**:12358. doi:10.1038/s41598-020-69096-7

Stebbins MJ, Gastfriend BD, Canfield SG, Lee M-SS, Richards D, Faubion MG, Li W-JJ, Daneman R, Palecek SP, Shusta E V. 2019. Human pluripotent stem cell–derived brain pericyte–like cells induce blood-brain barrier properties. *Sci Adv* **5**:eaau7375. doi:10.1126/sciadv.aau7375

Stenman JM, Rajagopal J, Carroll TJ, Ishibashi M, McMahon J, McMahon AP. 2008. Canonical Wnt Signaling Regulates Organ-Specific Assembly and Differentiation of CNS Vasculature. *Science (80-)* **322**:1247–1250. doi:10.1126/science.1164594

Syvänen S, Lindhe Ö, Palner M, Kornum BR, Rahman O, Långström B, Knudsen GM, Hammarlund-Udenaes M, Lindhe O, Palner M, Kornum BR, Rahman O, Långström B, Knudsen GM, Hammarlund-Udenaes M. 2009. Species differences in blood-brain barrier

transport of three positron emission tomography radioligands with emphasis on P-glycoprotein transport. *Drug Metab Dispos* **37**:635–643. doi:10.1124/dmd.108.024745

Tran KA, Zhang X, Predescu D, Huang X, MacHado RF, Göthert JR, Malik AB, Valyi-Nagy T, Zhao Y-YY. 2016. Endothelial β-Catenin Signaling Is Required for Maintaining Adult Blood-Brain Barrier Integrity and Central Nervous System Homeostasis. *Circulation* **133**:177–86. doi:10.1161/CIRCULATIONAHA.115.015982

Uchida Y, Ohtsuki S, Katsukura Y, Ikeda C, Suzuki T, Kamiie J, Terasaki T. 2011. Quantitative targeted absolute proteomics of human blood-brain barrier transporters and receptors. *J Neurochem* **117**:333–345. doi:10.1111/j.1471-4159.2011.07208.x

Umans RA, Henson HE, Mu F, Parupalli C, Ju B, Peters JL, Lanham KA, Plavicki JS, Taylor MR. 2017. CNS angiogenesis and barriergenesis occur simultaneously. *Dev Biol* **425**:101–108. doi:10.1016/j.ydbio.2017.03.017

Vallon M, Yuki K, Nguyen TD, Chang J, Yuan J, Siepe D, Miao Y, Essler M, Noda M, Garcia KC, Kuo CJ. 2018. A RECK-WNT7 Receptor-Ligand Interaction Enables Isoform-Specific Regulation of Wnt Bioavailability. *Cell Rep* **25**:339-349.e9. doi:10.1016/j.celrep.2018.09.045

Vanhollebeke B, Stone OA, Bostaille N, Cho C, Zhou Y, Maquet E, Gauquier A, Cabochette P, Fukuhara S, Mochizuki N, Nathans J, Stainier DYR. 2015. Tip cell-specific requirement for an atypical Gpr124- and Reck-dependent Wnt/β-catenin pathway during brain angiogenesis. *Elife* **4**:1–25. doi:10.7554/eLife.06489

Vanlandewijck M, He L, Mäe MA, Andrae J, Ando K, Del Gaudio F, Nahar K, Lebouvier T, Laviña B, Gouveia L, Sun Y, Raschperger E, Räsänen M, Zarb Y, Mochizuki N, Keller A, Lendahl U, Betsholtz C. 2018. A molecular atlas of cell types and zonation in the brain vasculature. *Nature* **554**:475–480. doi:10.1038/nature25739

Vatine GD, Al-Ahmad A, Barriga BK, Svendsen S, Salim A, Garcia L, Garcia VJ, Ho R, Yucer N, Qian T, Lim RG, Wu J, Thompson LM, Spivia WR, Chen Z, Van Eyk J, Palecek SP, Refetoff S, Shusta E V, Svendsen CN. 2016. Modeling Psychomotor Retardation using iPSCs from MCT8-Deficient Patients Indicates a Prominent Role for the Blood-Brain Barrier. *Cell Stem Cell* 1–13. doi:10.1016/j.stem.2017.04.002

Vatine GD, Barrile R, Workman MJ, Chen Z, Eyk J Van, Svendsen CN, Vatine GD, Barrile R, Workman MJ, Sances S, Barriga BK, Spivia WR, Chen Z, Eyk J Van, Svendsen CN. 2019. Human iPSC-Derived Blood-Brain Barrier Chips Resource Chips Enable Disease Modeling and Personalized Medicine Applications. *Stem Cell* **24**:995-1005.e6. doi:10.1016/j.stem.2019.05.011

Wang Y, Rattner A, Zhou Y, Williams J, Smallwood PM, Nathans J. 2012. Norrin/Frizzled4 signaling in retinal vascular development and blood brain barrier plasticity. *Cell* **151**:1332–1344. doi:10.1016/j.cell.2012.10.042

Wang Y, Sabbagh MF, Gu X, Rattner A, Williams J, Nathans J. 2019. Beta-catenin signaling regulates barrier- specific gene expression in circumventricular organ and ocular

1120   vasculatures. *Elife* **8**:1–36. doi:10.7554/eLife.43257

1121 Workman MJ, Svendsen CN. 2020. Recent advances in human iPSC-derived models of the
1122   blood-brain barrier. *Fluids Barriers CNS* **17**:1–10. doi:10.1186/s12987-020-00191-7

1123 Yates AD, Achuthan P, Akanni W, Allen JJJ, Allen JJJ, Alvarez-Jarreta J, Amode MR, Armean
1124   IM, Azov AG, Bennett R, Bhai J, Billis K, Boddu S, Marugán JC, Cummins C, Davidson C,
1125   Dodiya K, Fatima R, Gall A, Giron CG, Gil L, Grego T, Haggerty L, Haskell E, Hourlier T,
1126   Izuogu OG, Janacek SH, Juettemann T, Kay M, Lavidas I, Le T, Lemos D, Martinez JG,
1127   Maurel T, McDowall M, McMahon A, Mohanan S, Moore B, Nuhn M, Oheh DN, Parker
1128   A, Parton A, Patricio M, Sakthivel MP, Abdul Salam AI, Schmitt BM, Schuilenburg H,
1129   Sheppard D, Sycheva M, Szuba M, Taylor K, Thormann A, Threadgold G, Vullo A, Walts
1130   B, Winterbottom A, Zadissa A, Chakiachvili M, Flint B, Frankish A, Hunt SE, IIsley G,
1131   Kostadima M, Langridge N, Loveland JE, Martin FJ, Morales J, Mudge JM, Muffato M,
1132   Perry E, Ruffier M, Trevanion SJ, Cunningham F, Howe KL, Zerbino DR, Flicek P. 2019.
1133   Ensembl 2020. *Nucleic Acids Res* **48**:D682–D688. doi:10.1093/nar/gkz966

1134 Ye X, Wang Y, Cahill H, Yu M, Badea TC, Smallwood PM, Peachey NS, Nathans J. 2009.
1135   Norrin, Frizzled-4, and Lrp5 Signaling in Endothelial Cells Controls a Genetic Program for
1136   Retinal Vascularization. *Cell* **139**:285–298. doi:10.1016/j.cell.2009.07.047

1137 Zhong S, Ding W, Sun L, Lu Y, Dong H, Fan X, Liu Z, Chen R, Zhang S, Ma Q, Tang F, Wu Q,
1138   Wang X. 2020. Decoding the development of the human hippocampus. *Nature* **577**:531–
1139   536. doi:10.1038/s41586-019-1917-5

1140 Zhou Y, Wang Y, Tischfield M, Williams J, Smallwood PM, Rattner A, Taketo MM, Nathans J.
1141   2014. Canonical WNT signaling components in vascular development and barrier
1142   formation. *J Clin Invest* **124**:3825–3846. doi:10.1172/JCI76431

1143 Zhou Y, Williams J, Smallwood PM, Nathans J. 2015. Sox7, Sox17, and Sox18 cooperatively
1144   regulate vascular development in the mouse retina. *PLoS One* **10**:1–22.
1145   doi:10.1371/journal.pone.0143650

1146

FIGURES AND FIGURE LEGENDS
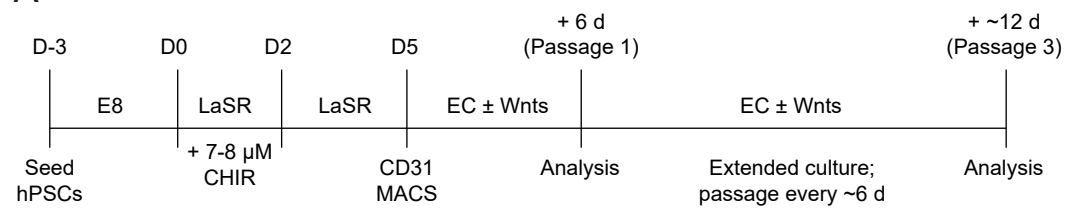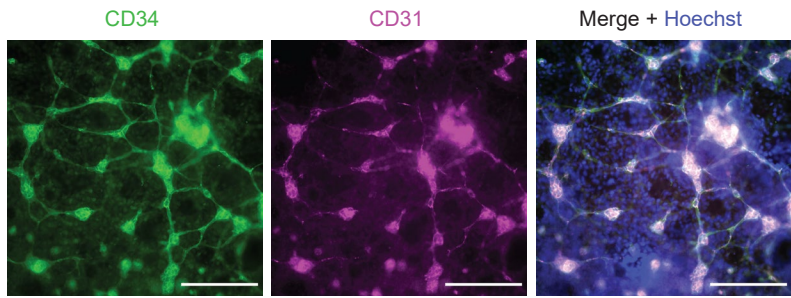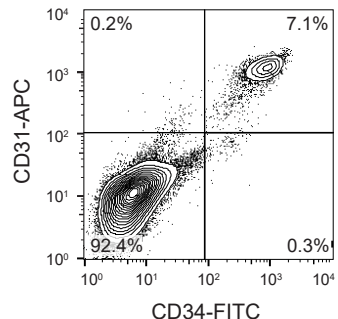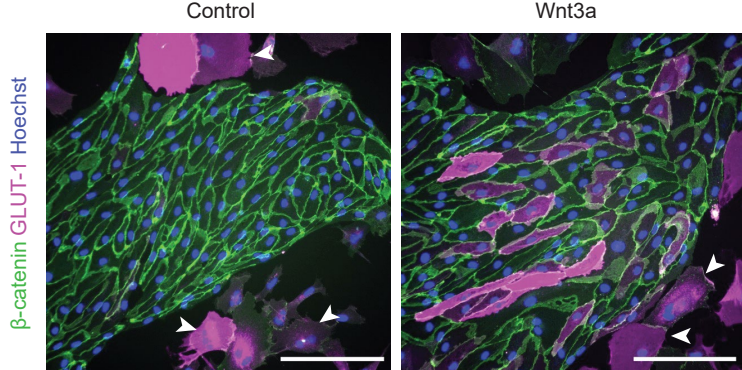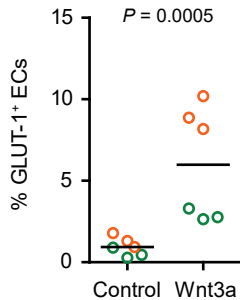
Figure 1. hPSC-derived endothelial progenitors as a model for studying Wnt-mediated barriergenesis.

(**A**) Overview of the endothelial differentiation and Wnt treatment protocol. (**B**) Immunocytochemistry analysis of CD34 and CD31 expression in D5 EPCs prior to MACS. Hoechst nuclear counterstain is overlaid in the merged image. Scale bars: 200 μm. (**C**) Flow cytometry analysis of CD34 and CD31 expression in D5 EPCs prior to MACS. (**D**) Immunocytochemistry analysis of β-catenin and GLUT-1 expression in Passage 1 ECs treated with Wnt3a or control. Hoechst nuclear counterstain is overlaid. Arrowheads indicate smooth muscle-like cells (SMLCs). Scale bars: 200 μm. (**E**) Quantification of the percentage of GLUT-1$^+$ ECs in control- and Wnt3a-treated conditions. Points represent replicate wells from 2 independent differentiations of the IMR90-4

47

line, each differentiation indicated with a different color. Bars indicate mean values. P-value: Two-way

ANOVA.
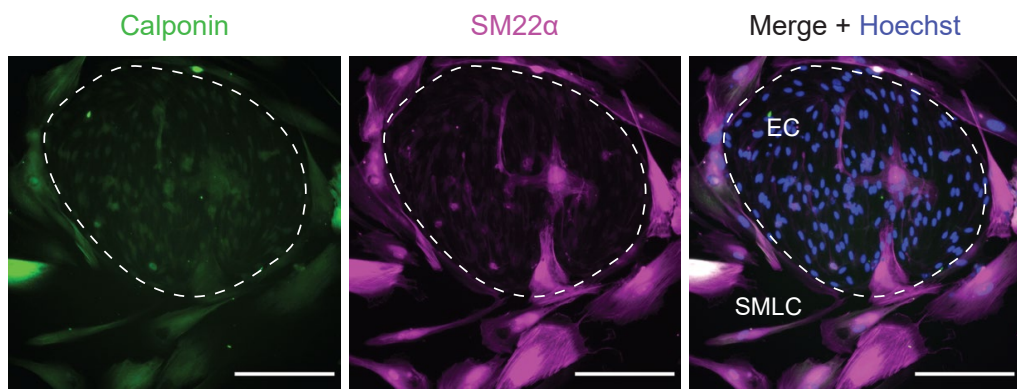
Figure 1–figure supplement 1. Smooth-muscle like cells (SMLCs). Immunocytochemistry analysis of calponin and smooth muscle protein 22-α (SM22α) in Passage 1 cultures containing ECs and SMLCs. Hoechst nuclear counterstain is overlaid in the merged image. Dashed area indicates an EC colony. Scale bars: 200 μm.

50
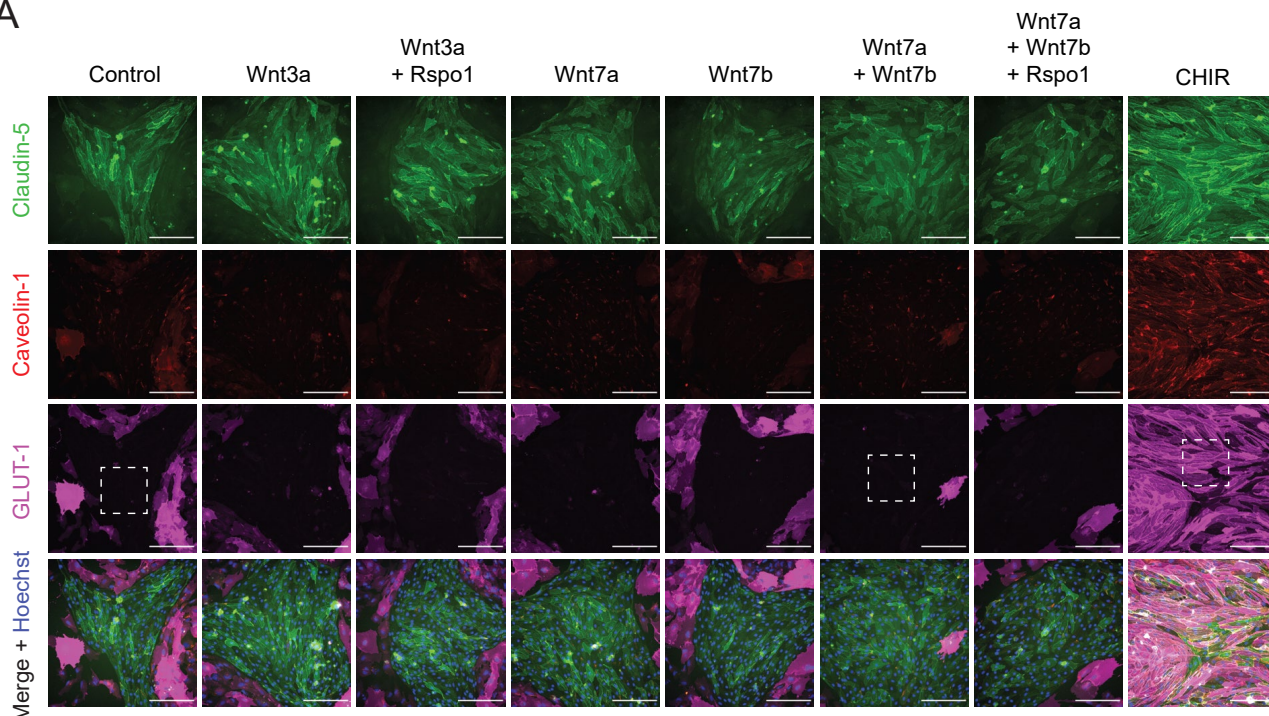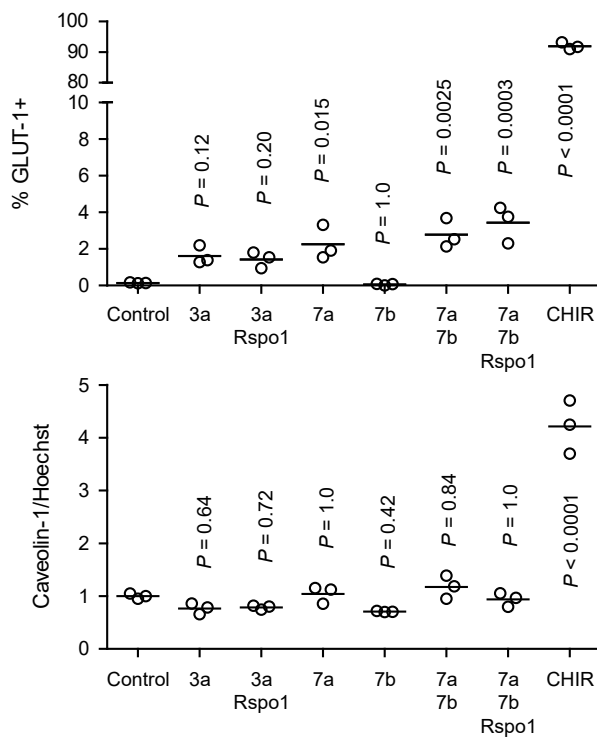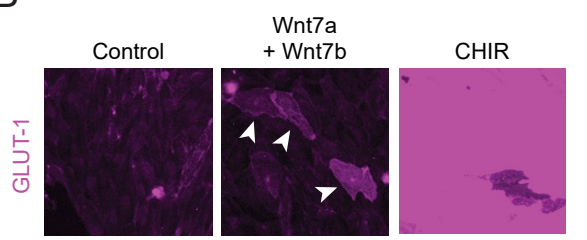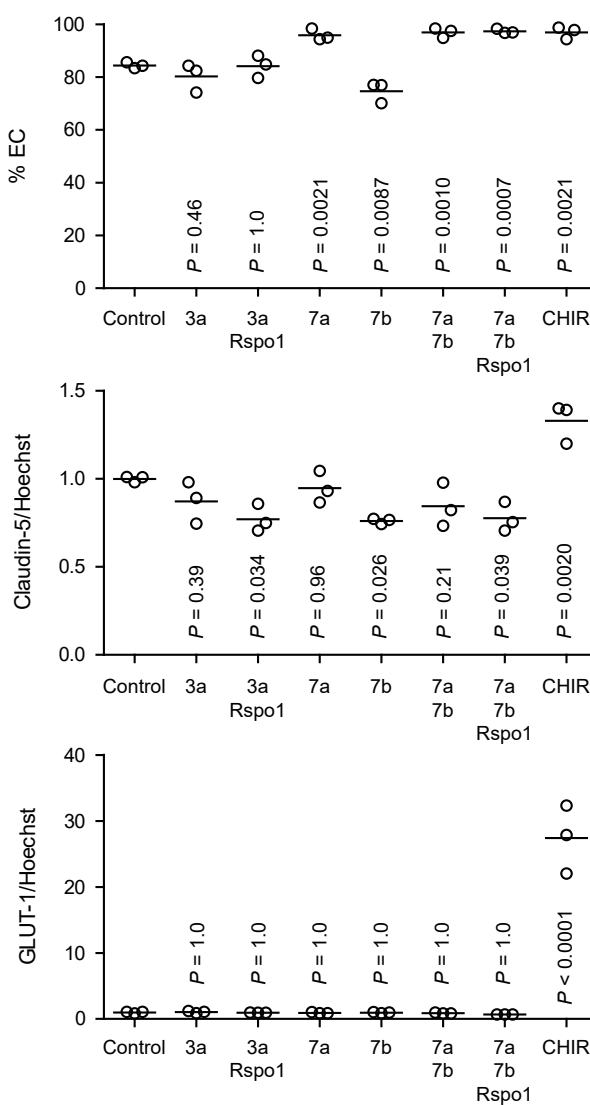
Figure 2. Effect of Wnt ligands and pathway modulators on endothelial properties. (A) Immunocytochemistry analysis of claudin-5, caveolin-1, and GLUT-1 expression in Passage 1 ECs treated with Wnt3a, Wnt3a + R-spondin 1 (Rspo1), Wnt7a, Wnt7b, Wnt7a + Wnt7b, Wnt7a + Wnt7b + Rspo1, CHIR, or control. Hoechst nuclear counterstain is overlaid in the merged images. Dashed boxes indicate fields displayed in (B). Scale bars: 200 μm. **(B)** Immunocytochemistry analysis of GLUT-1 expression in the fields indicated with dashed boxes in (A) from the control and Wnt7a + Wnt7b conditions. To visualize weak GLUT-1 immunoreactivity in Wnt7a + Wnt7b-treated ECs, a linear brightness/contrast adjustment was applied identically to the three fields but differs from that of the images shown in (A). Arrowheads indicate GLUT-1$^+$ ECs. **(C)** Quantification of images from the conditions described in (A) for percentage of ECs (claudin-5$^+$ cells relative to total nuclei), GLUT-1$^+$ ECs (relative to total claudin-5$^+$ ECs), and mean fluorescence intensity of claudin-5, caveolin-1, and GLUT-1 normalized to Hoechst mean fluorescence intensity within the area of claudin-5$^+$ ECs only. Points represent replicate wells from one differentiation of the IMR90-4 line and bars indicate mean values. For the fluorescence intensity plots, values were normalized such that the mean of the control condition equals 1. P-values: ANOVA followed by Dunnett's test versus control.
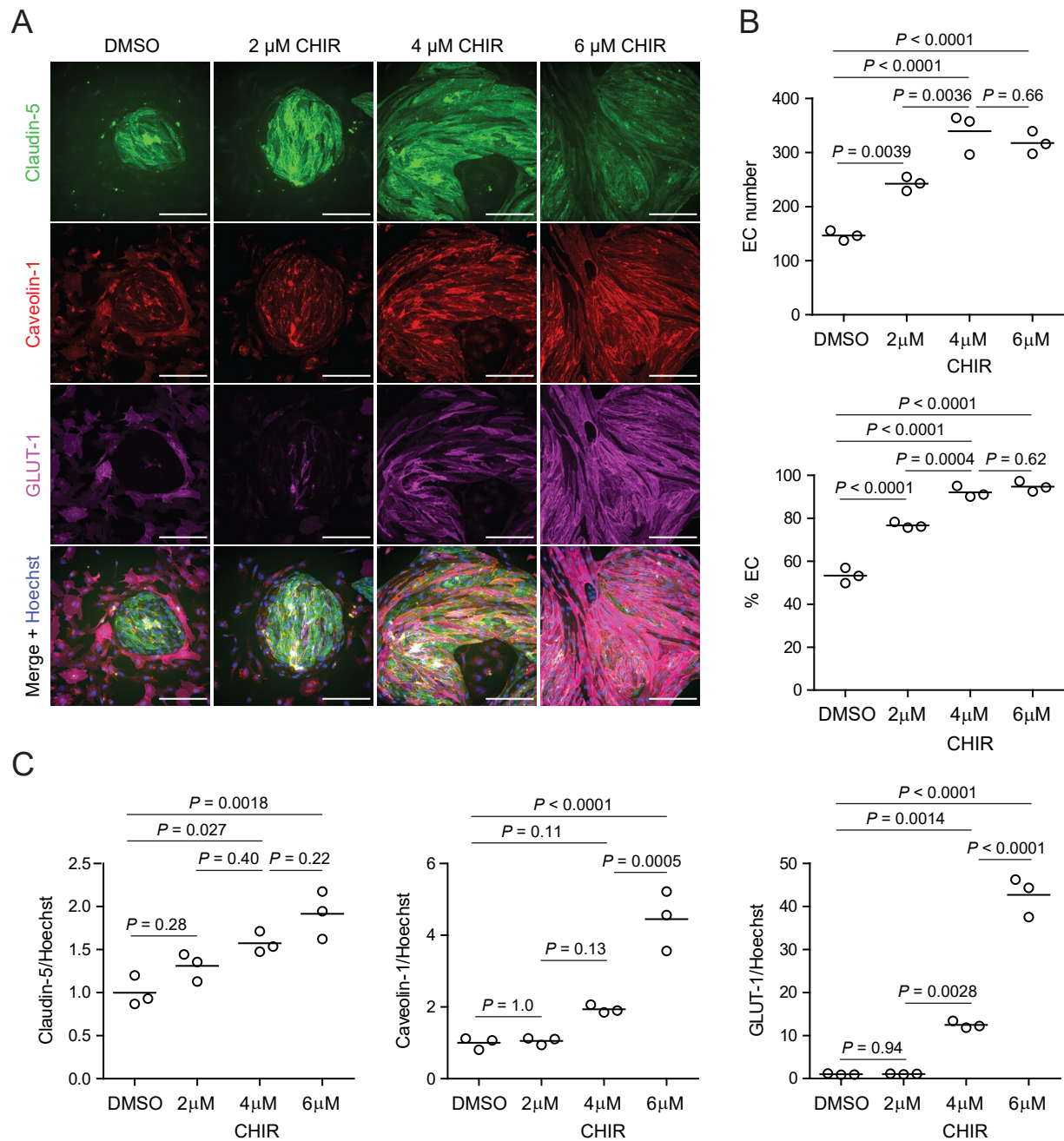
Figure 2–figure supplement 1. Dose-dependent effects of CHIR on endothelial properties. (A)

Immunocytochemistry analysis of claudin-5, caveolin-1, and GLUT-1 expression in Passage 1 ECs treated with 2 µM, 4 µM, or 6 µM CHIR, or DMSO vehicle control. Hoechst nuclear counterstain is overlaid in the merged images. Scale bars: 200 µm. **(B)** Quantification of images from the conditions described in (A) for number of ECs per 20× field and percentage of ECs (claudin-5^{+} cells relative to total nuclei). Points represent replicate wells from one differentiation of the IMR90-4 line and bars indicate mean values. P-values: ANOVA followed by Tukey's HSD test. **(C)** Quantification of claudin-5, caveolin-1, and GLUT-1 mean fluorescence intensity

normalized to Hoechst mean fluorescence intensity within the area of claudin-5$^+$ ECs only. Points represent

replicate wells from one differentiation of the IMR90-4 line. Bars indicate mean values, with values normalized

such that the mean of the DMSO condition equals 1. P-values: ANOVA followed by Tukey's HSD test.
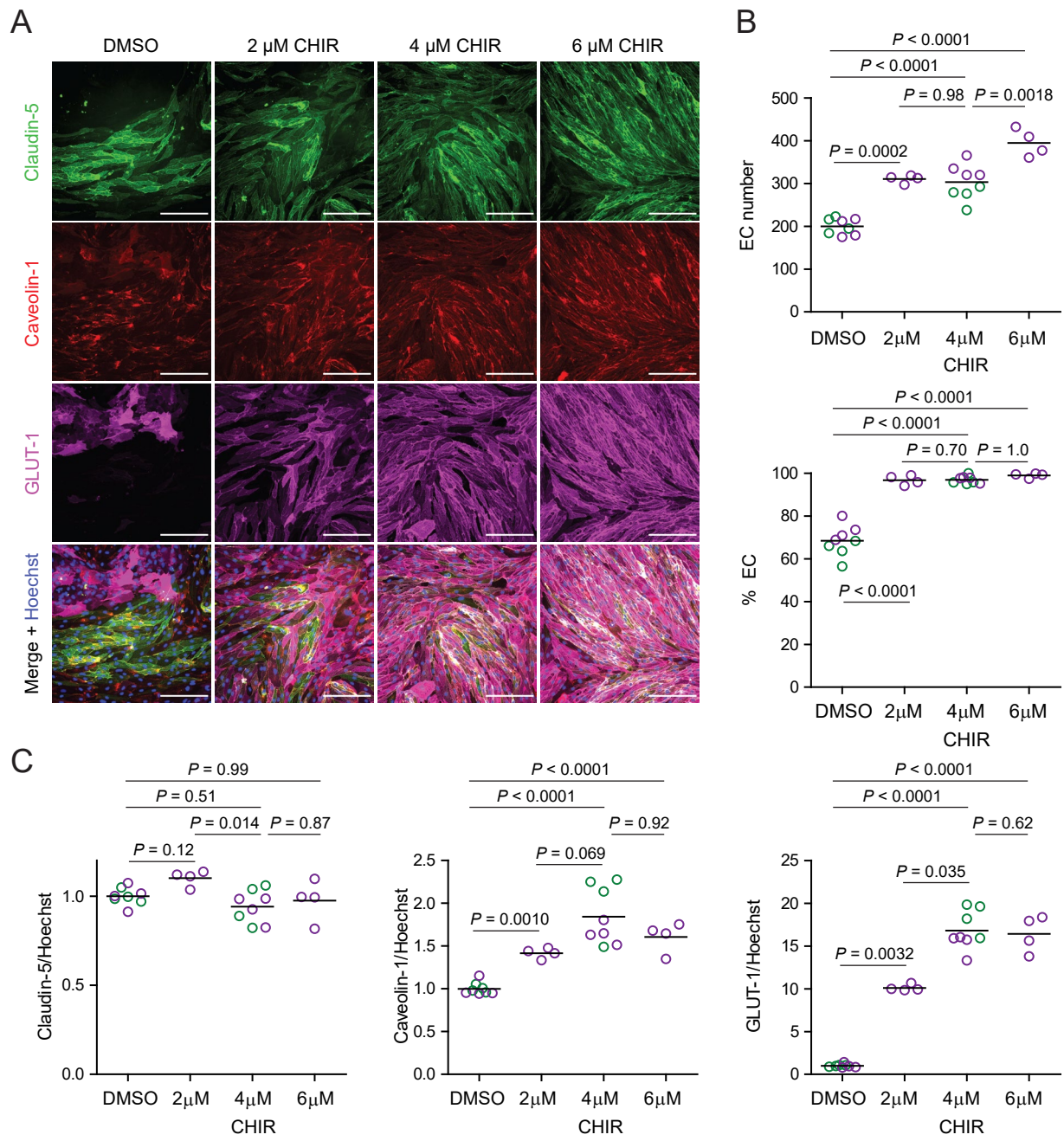
Figure 2–figure supplement 2. CHIR-mediated effects in an additional hPSC line. (A)

Immunocytochemistry analysis of claudin-5, caveolin-1, and GLUT-1 expression in Passage 1 ECs

differentiated from the WTC11 iPSC line treated with 2 μM, 4 μM, or 6 μM CHIR, or DMSO vehicle control.

Hoechst nuclear counterstain is overlaid in the merged images. Scale bars: 200 μm. **(B)** Quantification of

images from the conditions described in (A) for number of ECs per 20× field and percentage of ECs (claudin-5[+]

cells relative to total nuclei). Points represent replicate wells from 1–2 differentiations of the WTC11 line and

bars indicate mean values, each differentiation indicated with a different color. P-values: Two-way ANOVA

followed by Tukey's HSD test. **(C)** Quantification of claudin-5, caveolin-1, and GLUT-1 mean fluorescence intensity normalized to Hoechst mean fluorescence intensity within the area of claudin-5$^+$ ECs only. Points represent replicate wells from 1–2 differentiations of the WTC11 line, each differentiation indicated with a different color. Bars indicate mean values, with values normalized within each differentiation such that the mean of the DMSO condition equals 1. P-values: Two-way ANOVA followed by Tukey's HSD test on unnormalized data.
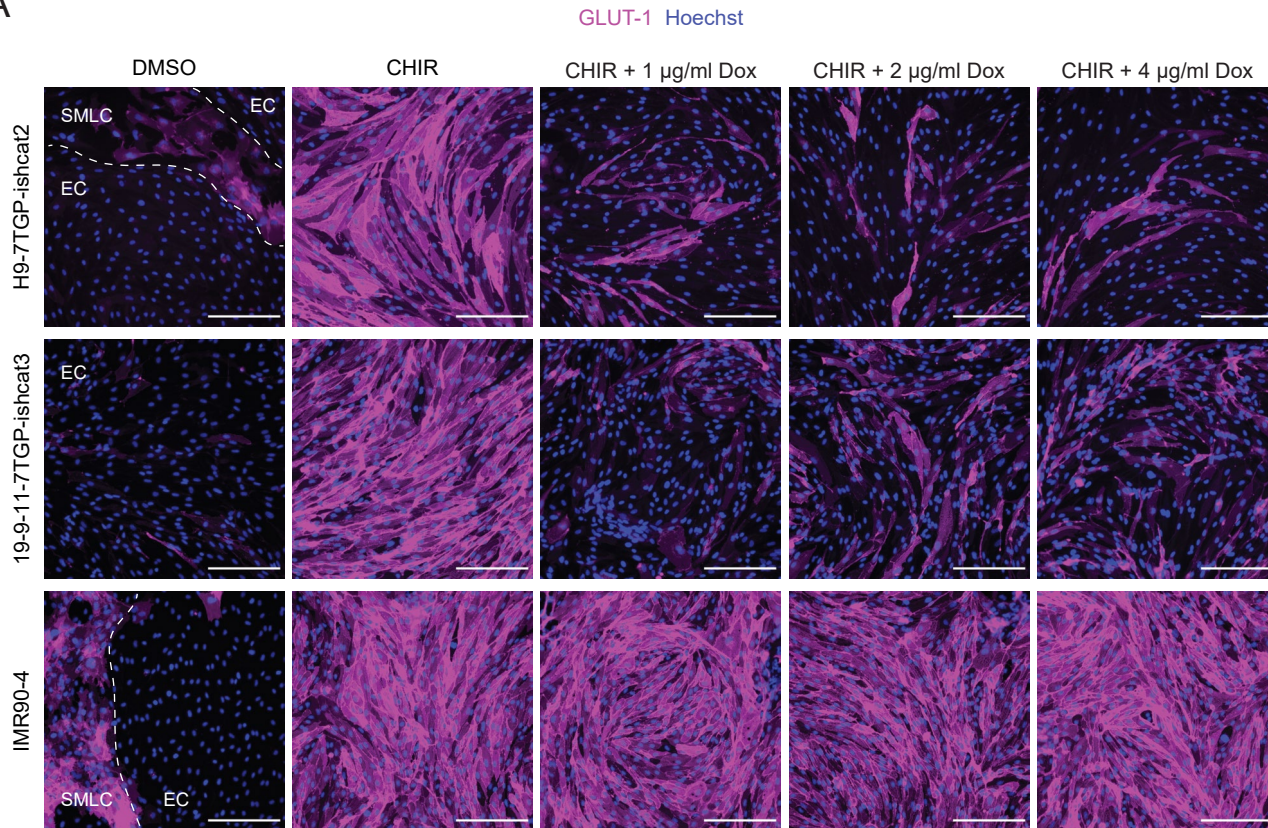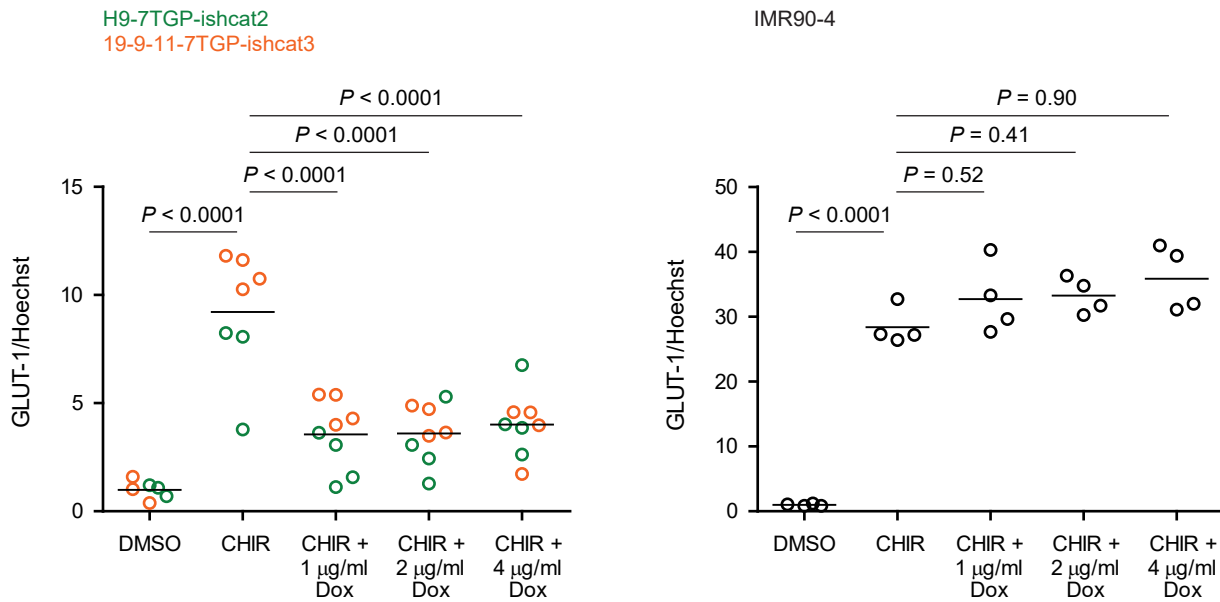
Figure 2–figure supplement 3. β-catenin-dependence of CHIR-mediated GLUT-1 induction. (A)

Immunocytochemistry analysis of GLUT-1 expression in Passage 1 ECs treated with DMSO, CHIR, or CHIR + doxycycline (Dox) at 1, 2, or 4 μg/ml. Images from the H9-7TGP-ishcat2, 19-9-11-7TGP-ishcat3, and IMR90-4 lines are shown. Hoechst nuclear counterstain is overlaid. Dashed lines indicate borders between EC colonies

56

and SMLCs in the DMSO condition. Scale bars: 200 μm. **(B)** Quantification of images from the conditions described in (A) for GLUT-1 mean fluorescence intensity normalized to Hoechst mean fluorescence intensity within the area of ECs only. At left, points represent replicate wells from one differentiation of the H9-7TGP-ishcat line (green) and one differentiation of the 19-9-11-7TGP-ishcat3 line (orange). Bars indicate mean values, with values normalized within each differentiation such that the mean of the DMSO condition equals 1. P-values: Two-way ANOVA followed by Tukey's HSD test on unnormalized data. At right, points represent replicate wells from one differentiation of the IMR90-4 line. Bars indicate mean values, with values normalized such that the mean of the DMSO condition equals 1. P-values: ANOVA followed by Tukey's HSD test.
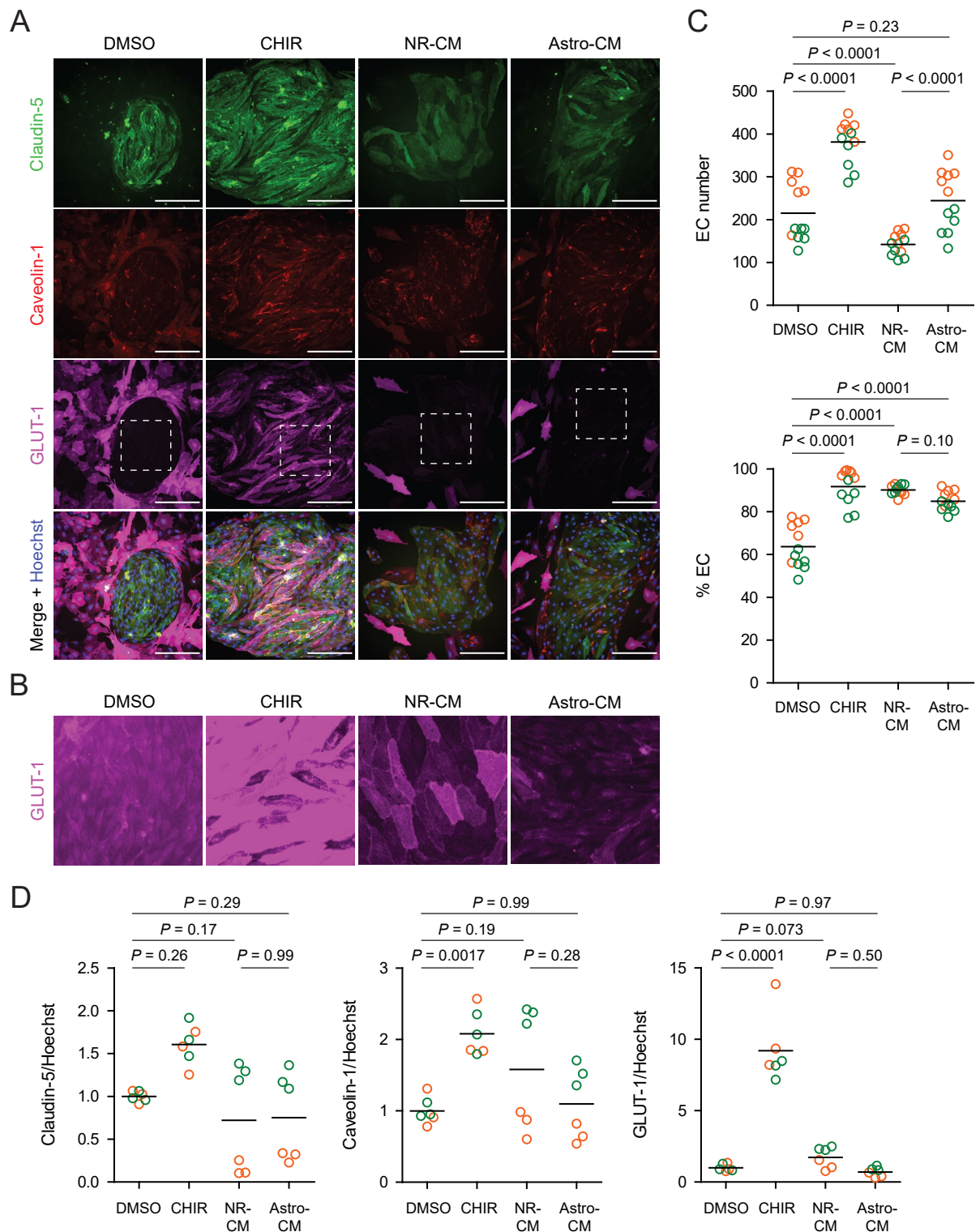
Figure 3. Effect of neural rosette- and astrocyte-conditioned media on endothelial properties. (A)

Immunocytochemistry analysis of claudin-5, caveolin-1, and GLUT-1 expression in Passage 1 ECs treated with

DMSO, CHIR, neural rosette-conditioned medium (NR-CM), or astrocyte-conditioned medium (Astro-CM).

58

Hoechst nuclear counterstain is overlaid in the merged images. Dashed boxes indicate fields displayed in (B). Scale bars: 200 μm. **(B)** Immunocytochemistry analysis of GLUT-1 expression in the fields indicated with dashed boxes in (A). A linear brightness/contrast adjustment was applied identically to the four fields but differs from that of the images shown in (A). **(C)** Quantification of images from the conditions described in (A) for number of ECs per 20× field and percentage of ECs (claudin-5$^+$ cells relative to total nuclei). Points represent replicate wells from two independent differentiations of the IMR90-4 line, each differentiation indicated with a different color. Bars indicate mean values. P-values: Two-way ANOVA followed by Tukey's HSD test. **(D)** Quantification of claudin-5, caveolin-1, and GLUT-1 mean fluorescence intensity normalized to Hoechst mean fluorescence intensity within the area of claudin-5$^+$ ECs only. Points represent replicate wells from two independent differentiations of the IMR90-4 line, each differentiation indicated with a different color. Bars indicate mean values, with values normalized within each differentiation such that the mean of the DMSO condition equals 1. P-values: Two-way ANOVA followed by Tukey's HSD test on unnormalized data.

Figure 4. Effect of CHIR on endothelial PLVAP expression. (A) Confocal immunocytochemistry analysis of VE-cadherin and PLVAP expression in Passage 1 ECs treated with DMSO or CHIR. Hoechst nuclear counterstain is overlaid. Eight serial confocal Z-slices with 1 μm spacing are shown. Scale bars: 50 μm. **(B)** Quantification of PLVAP and VE-cadherin area under the curve (AUC) of mean fluorescence intensity versus Z-position normalized to Hoechst AUC. Points represent replicate wells from 3 independent differentiations of the IMR90-4 line, each differentiation indicated with a different color. Bars indicate mean values, with values normalized within each differentiation such that the mean of the DMSO condition equals 1. P-values: Two-way ANOVA on unnormalized data.

60
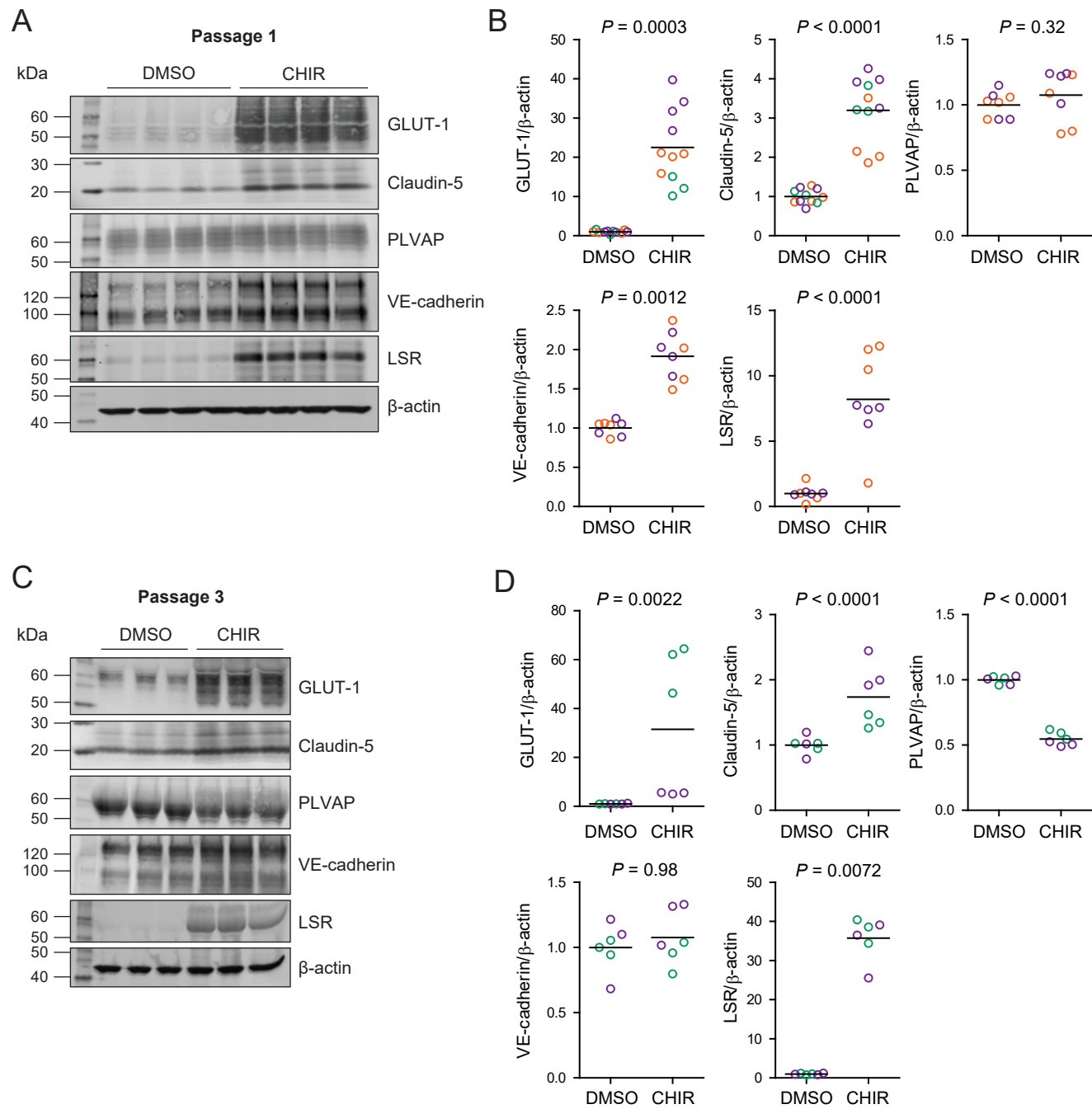
Figure 5. Effect of CHIR on protein expression in Passage 1 and Passage 3 ECs. (A) Western blots of Passage 1 ECs treated with DMSO or CHIR probed for GLUT-1, claudin-5, PLVAP, VE-cadherin, LSR, and β-actin. **(B)** Quantification of Western blots of Passage 1 ECs. GLUT-1, claudin-5, PLVAP, VE-cadherin, and LSR band intensities were normalized to β-actin band intensity. Points represent replicate wells from 2–3 independent differentiations of the IMR90-4 line, each differentiation indicated with a different color. Bars indicate mean values, with values normalized within each differentiation such that the mean of the DMSO condition equals 1. P-values: Two-way ANOVA on unnormalized data. **(C)** Western blots of Passage 3 ECs

treated with DMSO or CHIR probed for GLUT-1, claudin-5, PLVAP, VE-cadherin, LSR, and β-actin. **(D)**

Quantification of Western blots of passage 3 ECs. GLUT-1, claudin-5, PLVAP, VE-cadherin, and LSR band

intensities were normalized to β-actin band intensity. Points represent replicate wells from 2 independent

differentiations of the IMR90-4 line, each differentiation indicated with a different color. Bars indicate mean

values, with values normalized within each differentiation such that the mean of the DMSO condition equals 1.

P-values: Two-way ANOVA on unnormalized data.
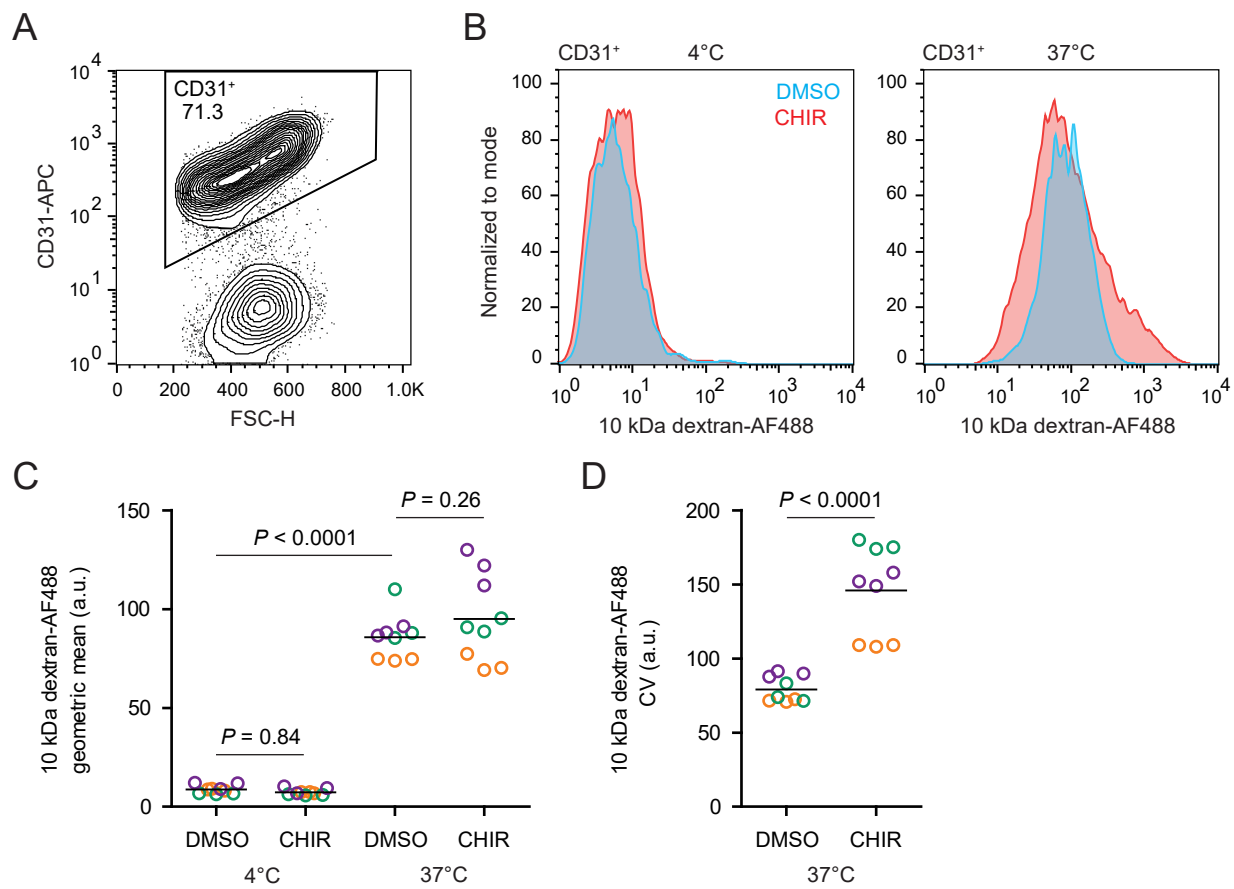
Figure 6. Fluid-phase endocytosis in CHIR- and DMSO-treated ECs. (A) Flow cytometry analysis of CD31 expression in Passage 1 ECs following the dextran internalization assay. CD31$^+$ cells were gated for further analysis. **(B)** Flow cytometry analysis of 10 kDa dextran-Alexa Fluor 488 (AF488) abundance in CD31$^+$ cells. Cells were treated with DMSO or CHIR for 6 d prior to the assay. Representative plots from cells incubated with dextran for 2 h at 4°C (left) and 37°C (right) are shown. **(C)** Quantification of 10 kDa dextran-AF488 geometric mean fluorescence intensity in CD31$^+$ cells. Treatment and assay conditions were as described in (B). Points represent replicate wells from 3 independent differentiations of the IMR90-4 line, each differentiation indicated with a different color. Bars indicate mean values. P-values: Two-way ANOVA followed by Tukey's HSD test. **(D)** Quantification of the coefficient of variation (CV) of 10 kDa dextran-AF488 fluorescence intensity in CD31$^+$ cells. Points represent replicate wells from 3 independent differentiations of the IMR90-4 line, each differentiation indicated with a different color. Bars indicate mean values. P-value: Two-way ANOVA.
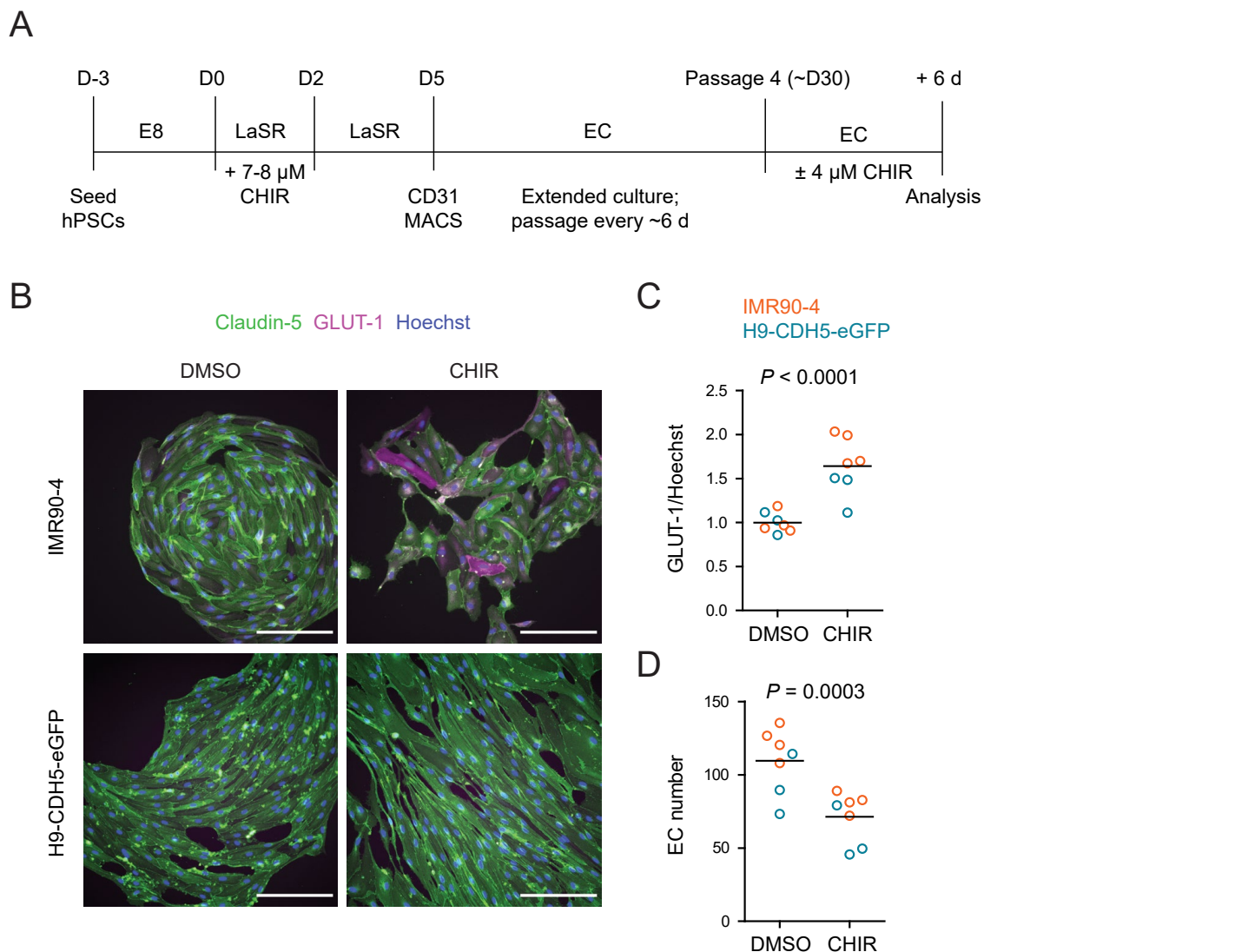
Figure 7. Effect of CHIR treatment in matured endothelium. (A) Overview of the endothelial differentiation, extended culture, and CHIR treatment protocol. **(B)** Immunocytochemistry analysis of claudin-5 and GLUT-1 expression in ECs treated with DMSO or CHIR as outlined in (A). Images from the IMR90-4 and H9-CDH5-eGFP lines are shown. Hoechst nuclear counterstain is overlaid. Scale bars: 200 μm. **(C)** Quantification of images from the conditions described in (B) for GLUT-1 mean fluorescence intensity normalized to Hoechst mean fluorescence intensity within the area of claudin-5$^+$ ECs only. Points represent replicate wells from one differentiation of the IMR90-4 line (orange) and one differentiation of the H9-CDH5-eGFP line (blue). Bars indicate mean values, with values normalized within each differentiation such that the mean of the DMSO condition equals 1. P-value: Two-way ANOVA on unnormalized data. **(D)** Quantification of images from the conditions described in (B) for number of ECs per 20× field. Points represent replicate wells

64

from one differentiation of the IMR90-4 line (orange) and one differentiation of the H9-CDH5-eGFP line

(blue). Bars indicate mean values. P-value: Two-way ANOVA.
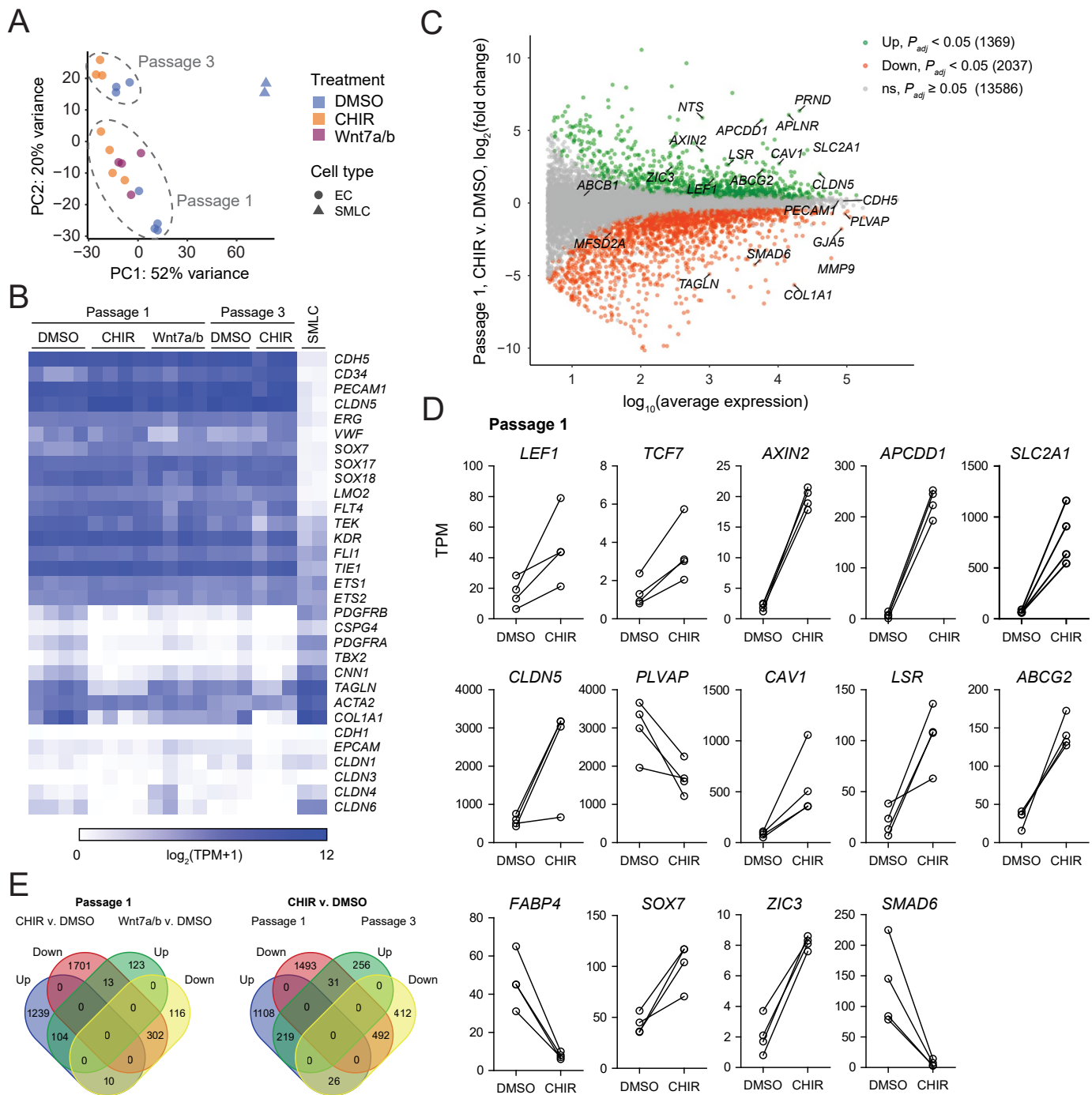
Figure 8. RNA-seq of DMSO-, CHIR-, or Wnt7a/b-treated ECs. (A) Principal component analysis of EC and SMLC whole-transcriptome data subject to variance stabilizing transformation by DESeq2. Points from Passage 1 ECs represent cells from 4 independent differentiations of the IMR90-4 line, points from Passage 3 ECs represent cells from 3 independent differentiations of the IMR90-4 line, and points from SMLCs represent 2 independent differentiations of the IMR90-4 line. Points are colored based on treatment: DMSO (blue), CHIR (orange), or Wnt7a/b (red). Data are plotted in the space of the first two principal components, with the

percentage of variance explained by principal component 1 (PC1) and principal component 2 (PC2) shown in axis labels. **(B)** Heat map of transcript abundance [$\log_2$(TPM+1)] for endothelial, mesenchymal, and epithelial genes across all samples. Abundance data for all transcripts is provided in Supplementary file 1. **(C)** Differential expression analysis of Passage 1 CHIR-treated ECs compared to Passage 1 DMSO-treated ECs. Differentially expressed genes (adjusted P-values < 0.05, DESeq2 Wald test with Benjamini-Hochberg correction) are highlighted in green (upregulated) and red (downregulated). The number of upregulated, downregulated, and non-significant (ns) genes are shown in the legend. Complete results of differential expression analysis are provided in Supplementary file 2. **(D)** Transcript abundance (TPM) of Wnt-regulated, barrier-related genes in Passage 1 DMSO- and CHIR-treated ECs. Points represent cells from 4 independent differentiations of the IMR90-4 line and lines connect points from matched differentiations. All genes shown were differentially expressed (adjusted P-values < 0.05, DESeq2 Wald test with Benjamini-Hochberg correction). P-values are provided in Supplementary file 2. **(E)** Venn diagrams illustrating the number of genes identified as upregulated or downregulated (adjusted P-values < 0.05, DESeq2 Wald test with Benjamini-Hochberg correction) in Passage 1 ECs treated with CHIR versus DMSO compared to Wnt7a/b versus DMSO (left), or ECs treated with CHIR versus DMSO at Passage 1 compared to Passage 3 (right). Gene lists are provided in Supplementary file 2.
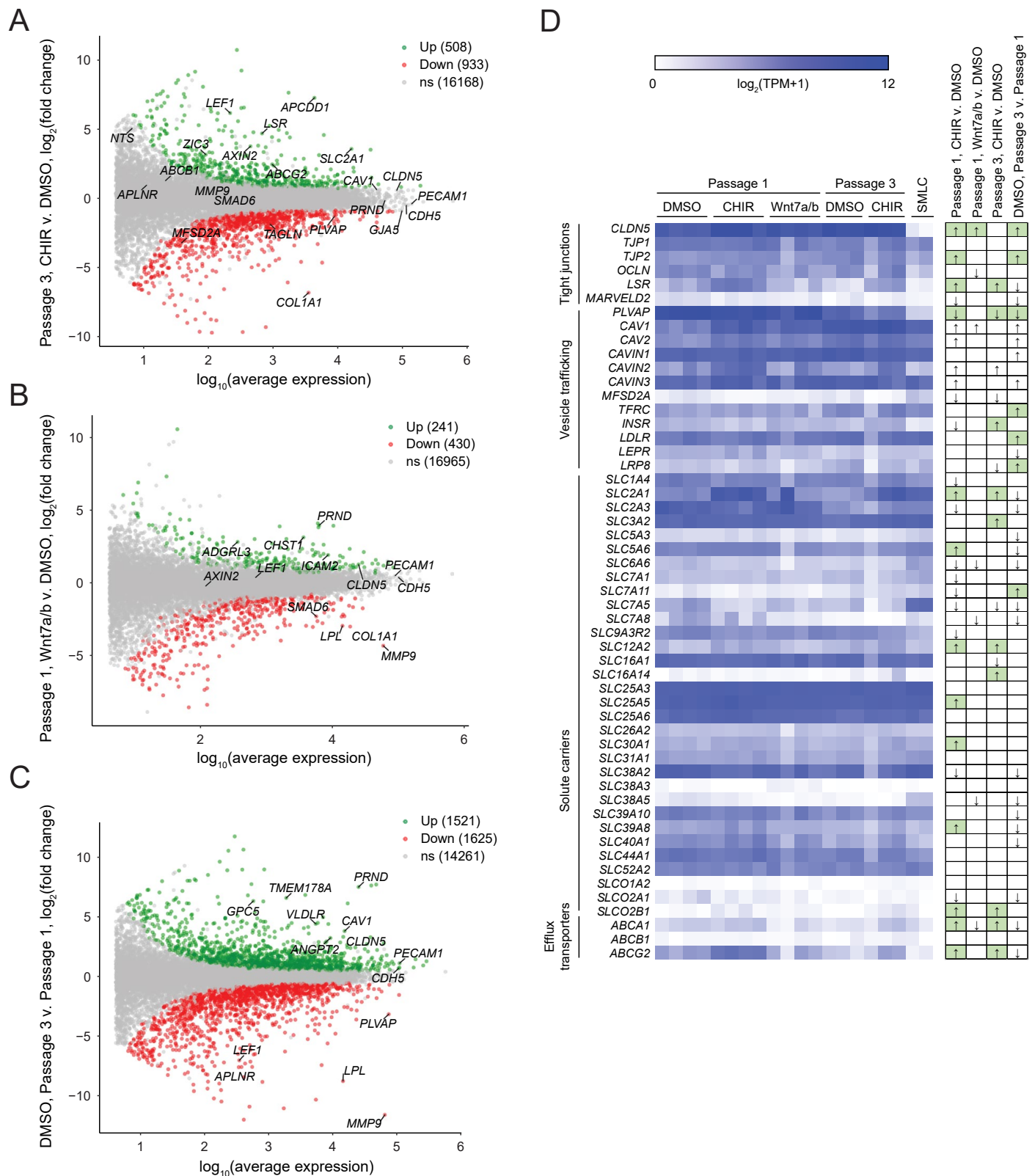
Figure 8–figure supplement 1. RNA-seq differential expression analyses. (A-C) Differential expression analysis of Passage 3 CHIR-treated ECs compared to Passage 3 DMSO-treated ECs (A), Passage 1 Wnt7a/b-treated ECs compared to Passage 1 DMSO-treated ECs (B), and Passage 3 DMSO-treated ECs compared to

Passage 1 DMSO-treated ECs (C). Differentially expressed genes (adjusted P-values < 0.05, DESeq2 Wald test with Benjamini-Hochberg correction) are highlighted in green (upregulated) and red (downregulated). The number of upregulated, downregulated, and non-significant (ns) genes are shown in the legends. Complete results of differential expression analyses are provided in Supplementary file 2. **(D)** Heat map of transcript abundance [$\log_2$(TPM+1)] for BBB genes encompassing tight junctions, vesicle trafficking components, and solute carriers, and efflux transporters. Solute carrier and efflux transporter genes that were expressed in human brain ECs at an average of >100 TPM in a meta-analysis of scRNA-seq datasets (Gastfriend et al., 2021) are included. Abundance data for all transcripts is provided in Supplementary file 1. At right, arrows indicate directionality of change for differentially expressed genes (adjusted P-values < 0.05, DESeq2 Wald test with Benjamini-Hochberg correction) for the four comparisons shown above. Changes with expected directionality for gain of CNS EC character have arrows highlighted in green.
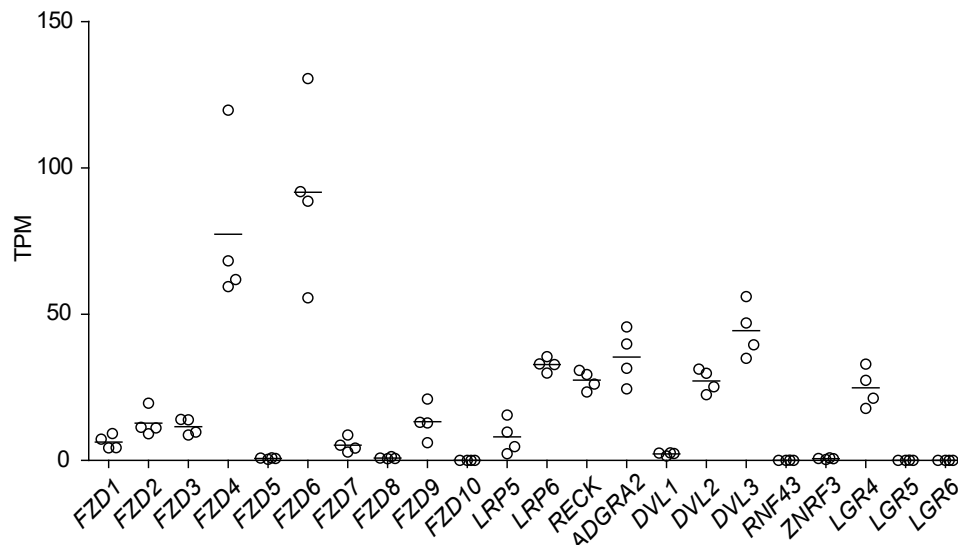
Figure 8–figure supplement 2. Expression of Wnt pathway components in naïve ECs. Abundance of transcripts (in transcripts per million, TPM) encoding Wnt receptors, co-receptors, and other pathway components in Passage 1 DMSO-treated ECs. Points represent cells from 4 independent differentiations of the IMR90-4 line. Bars indicate mean values. *ADGRA2* is also known as *GPR124*.

71
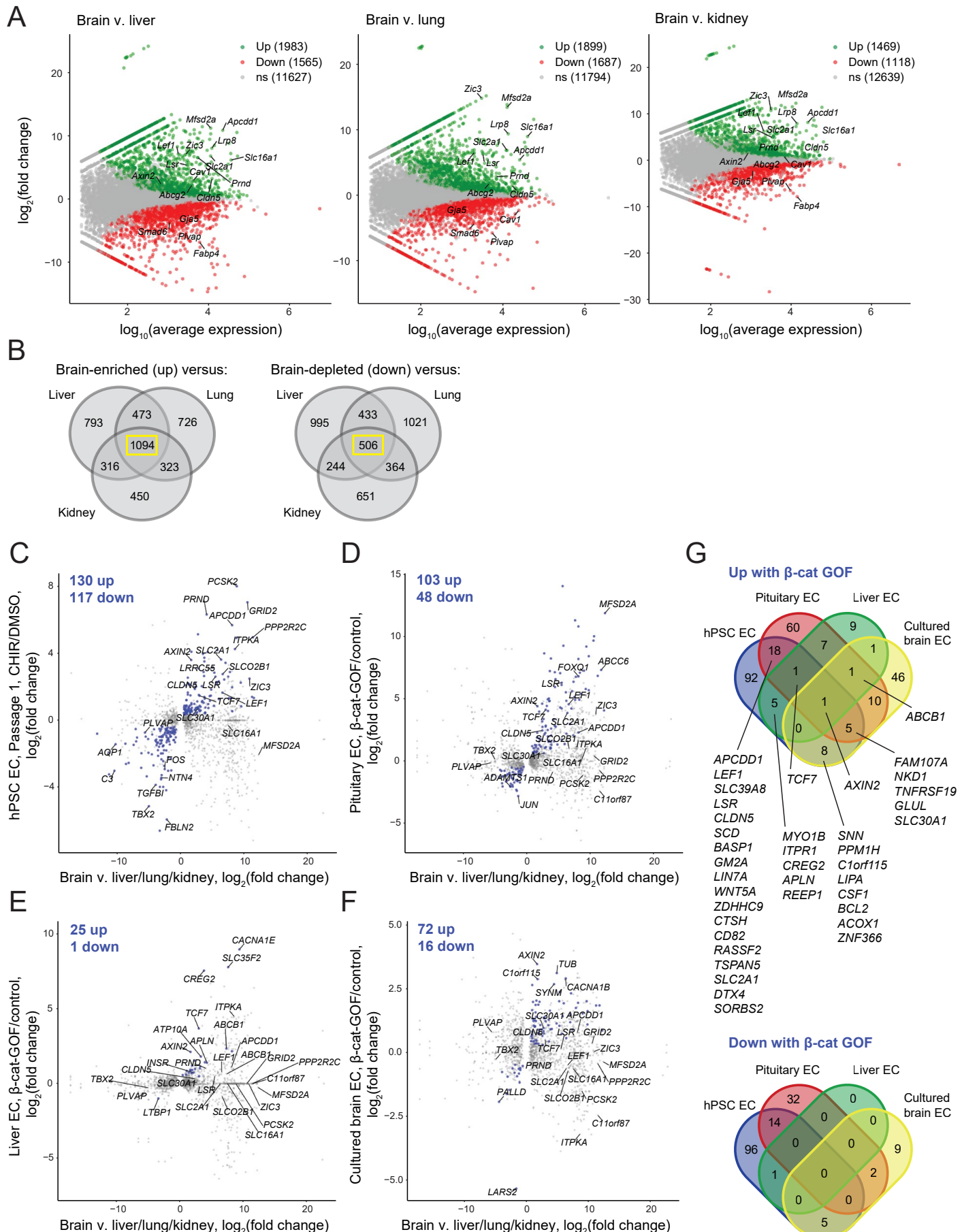
Figure 9. Identification of concordantly Wnt-regulated CNS EC-associated genes in RNA-seq data. (A) Differential expression analysis of P7 murine brain ECs compared to liver, lung, or kidney ECs (Sabbagh *et al.*, 2018). Differentially expressed genes (adjusted P-values < 0.05, DESeq2 Wald test with Benjamini-Hochberg correction) are highlighted in green (up, brain-enriched) and red (down, brain-depleted). The number of up, down, and non-significant (ns) genes are shown in the legends. **(B)** Venn diagrams illustrating the number of genes identified as brain EC-enriched (left) or brain EC-depleted (right) versus liver, lung, or kidney ECs (adjusted P-values < 0.05, DESeq2 Wald test with Benjamini-Hochberg correction). The 1094 genes enriched in brain ECs compared to each other organ, and the 506 genes depleted in brain ECs compared to each other organ, were used for subsequent analysis of the effects of Wnt activation in the various experimental contexts. **(C-F)** In each plot, the x-axis indicates average $\log_2$(fold change) of gene expression in brain ECs compared to liver, lung, and kidney ECs for the 1094 brain EC-enriched genes and 506 brain EC-depleted genes described in (B) with known mouse-human homology. Homologous human gene names are shown. The y-axes indicate differential expression [$\log_2$(fold change)] in Passage 1 CHIR-treated ECs compared to Passage 1 DMSO-treated ECs (C), in adult mouse pituitary ECs with stabilized β-catenin (gain-of-function, GOF) compared to controls (Wang *et al.*, 2019) (D), in adult mouse liver ECs with stabilized β-catenin compared to controls (Munji *et al.*, 2020) (E), or in cultured adult mouse brain ECs with stabilized β-catenin compared to controls (Sabbagh *et al.*, 2020) (F). Points are highlighted in blue if concordantly-regulated (upregulated in both comparisons or downregulated in both comparisons). Genes were identified as upregulated or downregulated based on adjusted P-values < 0.05, DESeq2 Wald test with Benjamini-Hochberg correction. **(G)** Venn diagrams illustrating the number of brain EC-enriched genes concordantly upregulated with β-catenin GOF (top) and the number of brain EC-depleted genes concordantly downregulated with β-catenin GOF (bottom) for the four comparisons shown in (C-F). Complete results of this analysis are provided in Supplementary file 3.